

# **New insights on the South China Sea Throughflow and its seasonal cycle: evaluation and analysis of a configuration at high-resolution including tides of the online closed-budget regional ocean model SYMPHONIE version 2.4**

5 Ngoc B. Trinh<sup>1,2</sup>, Marine Herrmann<sup>1,2</sup>, Caroline Ulses<sup>1,2</sup>, Patrick Marsaleix<sup>1</sup>, Thomas Duhaut<sup>1</sup>, To Duy Thai<sup>3</sup>, Claude Estournel<sup>1</sup>, R. Kipp Shearman<sup>4</sup>

<sup>1</sup>LEGOS (IRD/CNES/CNRS/UPS), 31400 Toulouse, France

<sup>2</sup>LOTUS Laboratory, University of Science and Technology of Hanoi (USTH), Vietnam Academy of Science and Technology (VAST), Hanoi, Vietnam

10 <sup>3</sup>Institute of Oceanography (IO), Vietnam Academy of Science and Technology (VAST), Nha Trang, Vietnam

<sup>4</sup>College of Earth, Ocean, and Atmospheric Sciences, Oregon State University, Corvallis, OR, United States

*Correspondence to:* Ngoc Bich Trinh (trinh-bich.ngoc@usth.edu.vn)

## **Short summary**

Seawater flows from the Pacific to the Indian oceans through the South China Sea (SCS) interocean straits, forming  
15 the South China Sea Throughflow. A high-resolution model was built to study SCS water, heat and salt budgets. The  
model performance is demonstrated by comparison with observations and other simulations. Important discards are  
observed if calculating offline, instead of online, lateral inflows and outflows of water, heat and salt. Over 2010-2018,  
SCS mainly receives water from the Luzon Strait, and releases it through the Mindoro, Karimata and Taiwan Straits.  
SCS surface interocean water exchanges are strongly driven by monsoon winds, which favor southwestward winter  
20 flows and northeastward summer flows.

## **Abstract**

The South China Sea Throughflow (SCSTF) connects the South China Sea (SCS) with neighboring seas and oceans,  
transferring surface water of the global thermohaline circulation between the Pacific and Indian oceans. A  
configuration of the SYMPHONIE ocean model at high resolution and including an explicit representation of tides is  
25 implemented over this region, and a simulation is analyzed over 2010-2018. Comparisons with in-situ and satellite  
data and other available simulations at coarser resolution show the good performance of the model in reproducing the  
spatial and temporal variability of the characteristics of surface dynamics and water masses over the SCS. The added  
value of an online computation of each term of the water, heat and salt SCS budgets (surface, lateral oceanic and river

fluxes and internal variations) is also quantitatively demonstrated: important discards are obtained with offline  
30 computation, with relative biases of ~40 % for lateral oceanic inflows and outflows.

The SCS water volume budget, including the SCSTF, is analyzed at the climatological and seasonal scales. The SCS  
receives on average a 4.5 Sv yearly water volume input, mainly from the Luzon Strait. It laterally releases this water  
to neighbouring seas, mainly to the Sulu Sea through the Mindoro Strait (49 %), to the East China Sea via the Taiwan  
Strait (28 %) and to the Java Sea through the Karimata Strait (22 %). The seasonal variability of this water volume  
35 budget is driven by lateral interocean exchanges. Surface interocean exchanges, especially at Luzon Strait, are all  
driven by monsoon winds which favor winter southwestward flows and summer northeastward surface flows.  
Exchanges through Luzon Strait deep layers show a stable sandwiched structure with vertically alternating inflows  
and outflows.

## 1. Introduction

40 The South China Sea (SCS, Fig. 1a), the largest marginal sea in the world, is subject to a wide range of forcings at  
different scales of both natural and anthropic origins. Its coasts are among the most densely populated regions in the  
world (CIESIN, 2018). The SCS is a source of subsistence for these populations (fishing, tourism, etc.) and is  
reciprocally affected by the harmful effects of human activities (pollution, resources overexploitation, etc.). The SCS  
plays an important role in regional and global ocean circulation and climate, transferring the surface water masses of  
45 the global thermohaline circulation between the Pacific and Indian oceans (Qu et al. 2005; Tozuka et al. 2007). It is  
therefore essential to understand, quantify and monitor the respective contributions of the lateral **oceanic**, atmospheric  
and continental fluxes in the SCS water, heat and salt budgets, and their interactions.

Ocean dynamics drive the transport and mixing of water masses, and are thus strongly involved in the functioning and  
variability of the water, heat and salt budgets of the SCS. They also determine the fate and functioning of matter in  
50 the marine compartment (planktonic ecosystems, contaminants, sediments). The SCS ocean circulation is regulated  
by a combination of factors, including the geometry of the zone, the tides, the connection with the Western Pacific  
and Eastern Indian oceans and the atmospheric forcing, from the daily to the seasonal and interannual scales (Wyrski,  
1961; Shaw and Chao, 1994; Metzger and Hurlburt, 1996; Gan et al. 2006). In the upper layer, the SCS basin scale  
circulation is mainly driven by the seasonal monsoon winds (Liu et al. 2002; Liu and Gan, 2017). In winter, strong  
55 northeasterly monsoon winds generate a cyclonic circulation in the surface and upper layers over the whole basin. In  
summer, weaker southwesterly monsoon winds lead to a cyclonic gyre in the north and an anticyclonic gyre in the  
south (Qu, 2000; Gan et al. 2016). At the interannual timescale, the SCS circulation is impacted by the El Niño  
Southern Oscillation (ENSO), via its effect on monsoon winds (Soden et al. 1999; Liu et al. 2014; Tan et al. 2016) but  
also via the direct propagation of ENSO oceanic signals from the Western Pacific Ocean through the Luzon Strait (Qu  
60 et al. 2004; Wang et al. 2006a). Other studies also suggested an impact of the Pacific Decadal Oscillation (PDO) on  
the SCS related to its effect on the intrusion of Western Pacific water (Yu and Qu, 2013) and on the atmospheric water

flux (Zeng et al. 2018). On the other side of the spectrum, the SCS is frequently crossed by tropical cyclones (Wang et al. 2007) that also affect ocean dynamics (Pan and Sun, 2013) and ecosystems (Liu et al. 2019). Last but not least, mesoscale to submesoscale structures play a significant role in the water masses dynamics and transports within the SCS (Liu et al. 2008; Chen et al. 2011; Nan et al. 2015; Da et al. 2019; Lin et al. 2020; Ni et al. 2021; Herrmann et al. 2023).

The SCS is connected with surrounding oceans and seas by several straits (Fig. 1a, white lines). The sills of Luzon and Mindoro Straits are 3000 m and 400 m deep respectively, the other straits are less than 100 m deep. The Luzon Strait – the largest and deepest interocean strait of the zone – is the main pathway of seawater from the Pacific Ocean into the SCS (Wyrki, 1961). Besides, the SCS exchanges seawater with the East China Sea through the Taiwan Strait, with the Sulu Sea through the Straits of Balabac and Mindoro, with the Java Sea and Andaman Sea (Indian Ocean) through Karimata and Malacca Straits. Mindoro, Balabac and Malacca Straits are particularly narrow, with widest passages not wider than 80, 55 and 20 km respectively. Based on numerical studies, satellite observations and long-term wind data analyzes, Qu et al. (2005) and Yu et al. (2007) revealed a circulation where Pacific Ocean water masses enter the SCS through the Luzon Strait and leave the basin through Taiwan, Karimata and Mindoro Straits, forming the South China Sea Throughflow (SCSTF). Those lateral transports are involved in the SCS cycle of water, heat and salt and interact with the atmospheric and continental components of this regional cycle. The SCS indeed receives net gains of freshwater and heat from the atmosphere and rivers. Estimates of net surface heat gain vary from 17 to 51 W m<sup>-2</sup> (Yang et al. 1999; Qu et al. 2004; Yu and Weller, 2007; Fang et al. 2009; Wang et al. 2019) and estimates of net water gain vary between 0.05 and 0.2 Sv (Qu et al. 2006; Fang et al. 2009).

Previous estimates of water volume, heat and salt transports at the straits were performed based on in-situ and satellite observations (Fang et al. 1991; Chu and Li, 2000; Chung et al. 2001; Wang et al. 2003; Tian et al. 2006; Yuan et al. 2008; Fang et al. 2010; Qu and Song, 2009; Sprintall et al. 2012; Susanto et al. 2013). However, in-situ estimates remain limited in space and time and are made complicated by the complex topography in the region. Numerical modeling is a relevant tool to complement in-situ and satellite measurements. Several modeling studies based on an integrated approach considering all terms of the budgets were performed, mainly focusing on water volume fluxes. Yaremchuk et al. (2009) provided estimates of upper water volume transport at Luzon, Taiwan, Mindoro and Karimata Straits issued from a reduced - gravity model. Wang et al. (2009), using a ~18 km resolution model, evaluated the seawater fluxes through all SCS interocean straits. In both studies, the inflow at Luzon was considered to be balanced by the outflows at other straits, i.e., internal variations were neglected, and the contribution from the atmosphere and rivers was not considered. Liu et al. (2011), Hsin et al. (2012), Tozuka et al. (2015), Wei et al. (2016) provided estimates of the SCS interocean water volume transports with higher resolution numerical models, but models configurations and assumptions did not allow to rigorously close the water volume budget. Several studies addressed the question of heat and salt fluxes. Qu et al. (2004) studied the whole depth water volume transports through Luzon, Mindoro and Sunda Straits and the upper heat budget of the zone, revealing that the surface heat flux is the primary heating process. However, their numerical study was carried out with a closed Taiwan Strait and a shallower Mindoro

Strait than reality, the inflow at Luzon was balanced by outflows at Mindoro and Sunda Straits, and the river heat flux was neglected. Qu et al. (2006), using a ~11 km resolution model, estimated the total water volume, heat and freshwater SCSTF, deducing surface heat and freshwater transports from the difference between the inflowing and outflowing fluxes of temperature and salinity. Fang et al. (2005, 2009) were the first, followed by Wang et al. (2019), to evaluate transports through all interocean straits of the SCS, using respectively ~18 km then ~7 km resolution models, but assuming that outflows compensate for inflows.

Those studies considerably improved our understanding of water volume, heat and salt transport through the SCS area. However, they were associated with several limitations. First, they assumed that the SCS is at equilibrium over the studied periods, i.e., that the same amount of water volume, heat and salt that enters the basin leaves it, and used this assumption to deduce atmosphere and rivers contributions. Though this assumption allows to close the budget at the first order, it does not account for possible internal variations and trends in the water volume, heat and salt contents of the SCS. Yet Zeng et al. (2014, 2018), using in situ measurements and satellite data, evidenced a freshening of the SCS from 2010 to 2012 followed by a salinification until 2016, suggesting an interannual variability in salt and/or water mass content. Moreover, very few studies examined jointly the water volume, heat and salt budgets, which is however necessary to provide consistent estimates of all the terms involved in those budgets and understand their interactions. Besides, using available (re)analysis to study those budgets requires to compute them offline, based on daily, weekly or even monthly distributed outputs, thus neglecting the turbulent term of temperature and salinity lateral transports. The error associated with this assumption requires to be assessed. Last, the model's resolution was rarely finer than 10 km, and they did not represent tides. As pointed out by Lin et al. (2020), models at higher resolution and including tides are necessary to represent the full range of temporal and spatial scales involved in the transport and mixing of water masses through the SCS. This includes the mesoscale to submesoscale eddies and structures of size smaller than 40 km (Da et al. 2019, Ni et al. 2021, Herrmann et al. 2023), as well as the detailed topography and dynamics of coastal areas and key straits, some of which less than 20 km wide, where interocean exchanges and strong internal tidal mixing occur (e.g. at Luzon Strait but also at narrow straits like Malacca, Mindoro and Balabac, Hatayama et al. 1996, Laurent 2008, Wang et al. 2016). Xu et al. (2022) indeed showed for the Atlantic ocean that using in a model combining a high resolution ( $1/50^\circ$ ) bathymetry and explicit tides improved the representation of internal waves, and consequently of the mesoscale sea surface height wavenumber spectrum over the tropical ocean. Sannino et al. (2009) and Chassignet et al. (2023) moreover pointed out the relevance of high-resolution bathymetry for the representation of interocean strait exchanges and mesoscale activity involved in western boundary currents, respectively.

Following this introduction, our first scientific objective is to better understand the role of the SCS in the global circulation and regional climate at different scales, i.e., daily, seasonal and interannual variability, by providing updated and consistent estimates at those scales of all the terms involved in the SCS water volume, heat and salt budgets: lateral oceanic, atmospheric and river fluxes and internal variations. For that, we developed a configuration of a regional ocean hydrodynamical model with a high spatial resolution (4 km) over the SCS and an explicit

representation of tides, in order to represent as realistically as possible the wide range of scales and processes involved  
 in the SCS dynamics and to study their contribution to SCS budgets. The water volume, heat and salt budgets have  
 been rigorously closed by performing online calculations of each term of those budgets, including incoming and  
 outgoing flows. The first objective of this paper is to present and evaluate in detail this modeling tool, that will be  
 used to study water volume, salt and heat budgets, and will be available to the community interested in addressing  
 scientific questions related to SCS ocean dynamics functioning, variability and influence. The second objective is to  
 perform a first analysis at the climatological and seasonal scales of water budget over the SCS and of its components,  
 i.e. river, atmospheric and oceanic lateral fluxes and internal variations.

The paper is organized as follows. Section 2 presents the hydrodynamical model, its high-resolution configuration  
 over the SCS and the observation data as well as the other numerical simulations at coarser resolution used for its  
 evaluation. The online computation of each term of the budgets are then detailed. The added-value of the online  
 computation compared to the offline computation is demonstrated in Section 3. The ability of the model to simulate  
 the SCS sea surface dynamics and water masses characteristics at different scales is evaluated in Section 4 through  
 comparisons with available in-situ and satellite observations and with other simulations. An evaluation and an analysis  
 of the water budget and its various components over the SCS are carried out on a climatological scale in Section 5,  
 and lateral exchanges at interocean straits, corresponding to the SCSTF, are examined in detail. Results are  
 summarized in Section 6, and an overview on the future applications of this high-resolution closed-budget modeling  
 tool is provided.

150

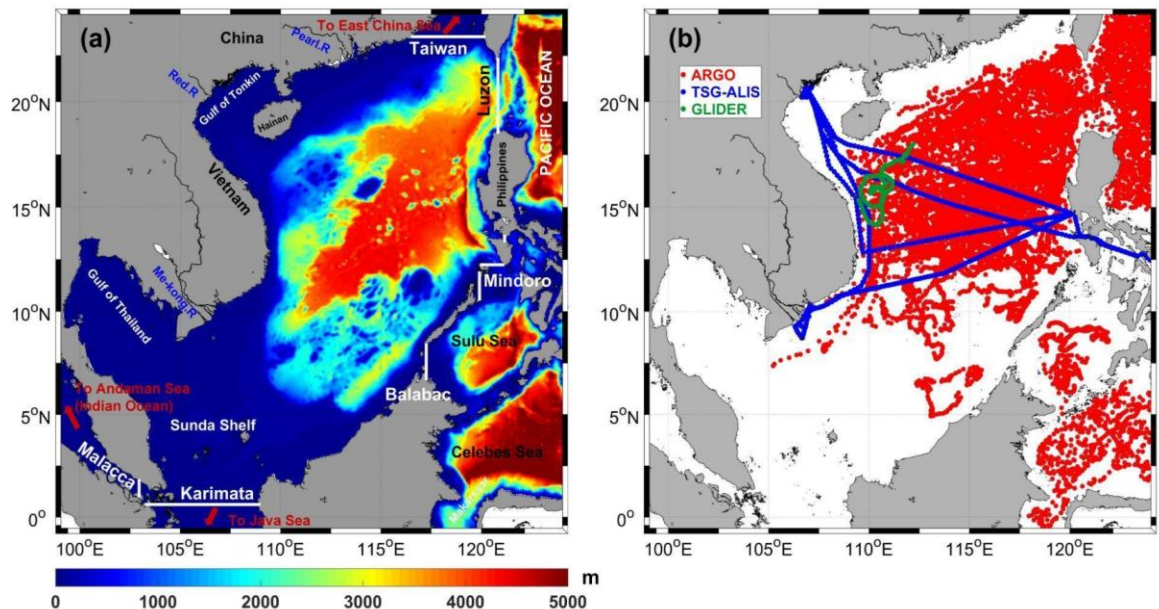


**Figure 1: (a) Computational domain bathymetry (m) and interocean straits (white lines). (b) Maps of Argo float trajectories in the SCS from January 2009 to December 2018 (red), TSG from R/V Alis trajectory from May to July 2014 (blue), and Glider trajectory from January to May 2017 (green).**

## 2. Materials and methods

### 155 2.1 The numerical model SYMPHONIE

#### 2.1.1 General presentation of the model

The 3-D ocean circulation model SYMPHONIE Marsaleix et al. (2008, 2019) is based on the Navier-Stokes primitive equations solved on an Arakawa curvilinear C-grid under the hydrostatic and Boussinesq approximations. The model makes use of an energy conserving finite difference method (Marsaleix et al. 2008), a forward-backward time stepping  
160 scheme, a Jacobian pressure gradient scheme (Marsaleix et al. 2009), the equation of state of Jackett et al. (2006), and the K-epsilon turbulence scheme with the implementation described in Costa et al. (2017). Horizontal advection and diffusion of tracers are computed using the QUICKEST scheme (Leonard, 1979) and vertical advection using a centered scheme. Horizontal advection and diffusion of momentum are each computed with a fourth order centered biharmonic scheme. The biharmonic viscosity of momentum is calculated according to a Smagorinsky-like  
165 formulation derived from Griffies and Hallberg (2000). The lateral open boundary conditions, based on radiation conditions combined with nudging conditions, are described in Marsaleix et al. (2006) and boundary conditions at river mouths are described in Nguyen-Duy et al. (2021). As in Estournel et al. (2021), To Duy et al. (2022) and Hermann et al. (2023), the VQS (vanishing quasi-sigma) vertical coordinate is used, allowing to avoid an excess of vertical levels in very shallow areas while maintaining an accurate description of the bathymetry and to reduce the  
170 truncation errors associated with the sigma coordinate.

#### 2.1.2 Model setup

The SYMPHONIE numerical configuration covers the whole SCS (99°E – 124°E, 0.6°S – 24°N, Fig. 1a), with a regular grid of 4 km horizontal resolution and 50 vertical levels in the deepest area. It is built from a bathymetry product merging GEBCO 2014 gridded bathymetry and digitalized nautical charts (Piton et al. 2020). Bathymetry  
175 ranges from 3 m to 5000 m in the studied area (Fig. 1a). The simulation runs from 01 January 2009 to 31 December 2018.

Initial and lateral oceanic boundary conditions for temperature, salinity, currents and sea level are provided by the daily outputs of the Global\_Analysis\_Forecast\_Phy\_001\_024 Global Ocean 1/12° physics analysis and forecast provided by Copernicus Marine Environment Monitoring Service (CMEMS) (<http://marine.copernicus.eu>; last access  
180 18 May 2023). The SYMPHONIE simulation departs from an initial state that is not at rest since it includes the currents from CMEMS 1/12° analysis. The spin-up time, whose main aim is to energetically adjust the initial physical fields provided by CMEMS to the specific constraints of the SYMPHONIE grid, lasts a few months. We therefore analyze the simulation over the period January 01, 2010 - December 31, 2018.

The SCS configuration includes 63 river mouths. Daily data were provided by the National Hydro-Meteorological  
185 Service of Vietnam for 11 rivers flowing in northern and central Vietnam (including the Red river). Monthly

climatology runoff issued from the CLS – INDESO project were provided for the other rivers, including the Mekong and Pearl rivers (Tranchant et al. 2016).

190 The atmospheric forcing is calculated from the bulk formulae of Large and Yeager (2004) using the European Centre for Medium Range Weather Forecasts (ECMWF) operational forecasts at 1/8° horizontal resolution and 3 hours temporal resolution, available at <https://www.ecmwf.int/>, last access 18 May 2023.

Open boundary tidal conditions are prescribed from FES2014b, the 2015 release of the FES (Finite Element Solution) global tide model (Carrere et al. 2016, Lyard et al., 2021), that assimilates altimetry satellite observations and tide gauges data. The data are freely available on Aviso website: <https://www.aviso.altimetry.fr/en/data/products/auxiliary-products/global-tide-fes.html> (last access 18 May 2023).  
195 The SCS configuration takes into account nine barotropic tidal components (in phase and altitude): M2, S2, N2, K2 (semi-diurnal tides), K1, P1, O1, Q1 (diurnal tides) and M4 (compound tide). The model is also forced by the astronomical plus the loading and self-attraction potentials (Lyard et al. 2006). Details and numerical issues related to tides can be found in Pairaud et al. (2008, 2010).

## 2.2 Fluxes calculation methods

200 We detail here the computation of each term of the water volume, heat and salt budgets over the whole SCS: internal content variations and surface, oceanic lateral and river fluxes. We compute lateral oceanic fluxes through the six interocean straits connecting the SCS to neighboring seas and oceans shown in Fig. 1a: Taiwan, Luzon, Mindoro, Balabac, Karimata and Malacca Straits. All the terms of the budget equations are computed online. The added-value of the online computation compared to the offline computation is presented in Section 3.

### 2.2.1 Water volume, heat and salt budgets equations

Water volume, heat and salt contents are rigorously conserved in SYMPHONIE, as shown below in Section 3 and Fig. 2: during each time step the variation (delta) of water volume, heat or salt content in the numerical ocean domain is equal to the net input from sources and sinks, i.e. the sum of fluxes from rivers, atmosphere and lateral oceanic boundaries.

#### 210 *Water volume budget*

The internal variation of water volume  $V$  over the SCS area between times  $t_1$  and  $t_2$  ( $\Delta V$ ) is equal to the integral between  $t_1$  and  $t_2$  of all water volume fluxes exchanged at the boundaries (atmosphere, rivers and lateral open ocean boundaries) of the SCS domain, taken as the sea zone limited by the six interocean straits shown in Fig. 1a:

$$\Delta V = V_{t_2} - V_{t_1} = \int_{t_1}^{t_2} (F_{w,lat} + F_{w,surf} + F_{w,riv}) dt \quad (Eq. 1)$$

215 where  $F_{w,lat}$ ,  $F_{w,surf}$  and  $F_{w,riv}$  are the net oceanic lateral, atmospheric surface and river water volume fluxes respectively. Here and in the following, positive fluxes correspond to inflows, and negative fluxes to outflows.

### **Heat budget**

The variation of heat content  $HC$  between times  $t_1$  and  $t_2$  ( $\Delta HC$ ) is equal to the sum of all heat fluxes exchanged at the boundaries of the SCS domain between  $t_1$  and  $t_2$ :

$$220 \quad \Delta HC = HC_{t_2} - HC_{t_1} = \int_{t_1}^{t_2} (F_{T,lat} + F_{T,surf} + F_{T,riv}) dt \quad (Eq. 2)$$

where  $F_{T,lat}$ ,  $F_{T,surf}$  and  $F_{T,riv}$  are the net oceanic lateral, atmospheric surface and river heat fluxes respectively, and  $HC$  is computed from:

$$HC = \rho_0 C_p \int_x \int_y \int_z T(x, y, z, t) dx dy dz \quad (Eq. 3)$$

225 with  $T$  the temperature (in °C),  $\rho_0$  the seawater density constant ( $1028 \text{ kg m}^{-3}$ ),  $C_p$  the seawater specific heat constant ( $3900 \text{ J kg}^{-1} \text{ °C}^{-1}$ ).

### **Salt budget**

230 The salinity of water going to or coming from to the atmosphere and the rivers is assumed to be zero, meaning that there is no input or output of salt from surface atmospheric fluxes and river runoff. It should be noted that evaporation, precipitation and river discharge are not sources/sinks of salt but are however sources/sinks of salinity for the ocean domain: although they do not affect the salt budget of the ocean domain, atmospheric and river fluxes do modify the salinity budget, as they affect the water volume budget. The variation of salt content between  $t_1$  and  $t_2$  ( $\Delta SC$ ) is thus equal to the sum of salt fluxes exchanged at the lateral oceanic boundaries of the SCS domain:

$$\Delta SC = SC_{t_2} - SC_{t_1} = \int_{t_1}^{t_2} F_{S,lat} dt \quad (Eq. 4)$$

where  $F_{S,lat}$  is the net salt flux at the lateral oceanic boundaries and  $SC$  is computed from:

$$235 \quad SC = \rho_0 \int_x \int_y \int_z S(x, y, z, t) dx dy dz \quad (Eq. 5)$$

with  $S$  the salinity.

### **2.2.2 Lateral fluxes through ocean open boundaries**

The total lateral water volume flux  $F_{w,lat}$  through the vertical section A of an open ocean boundary is computed in Sv ( $1 \text{ Sv} = 10^6 \text{ m}^3 \text{ s}^{-1}$ ) from:



240 
$$F_{w,lat} = \int_A v_t dA \quad (Eq. 6)$$

with  $v_t$  the current velocity normal to the transect and  $A$  the area of the section from the surface to bottom.

The lateral heat flux  $F_{T,lat}$  in PW (PW =  $10^{15}$  W) is computed from:

$$F_{T,lat} = \rho_0 C_p \int_A T v_t dA \quad (Eq. 7)$$

The lateral salt flux  $F_{S,lat}$  in Gg  $s^{-1}$  is computed from:

245 
$$F_{S,lat} = \rho_0 \int_A S v_t dA \quad (Eq. 8)$$

Inflowing and outflowing fluxes are also computed using the same equations, but for values of  $v_t > 0$  and  $v_t < 0$ , respectively:

$$F_{w,lat+} = \int_A v_t / (v_t > 0) dA \quad \text{and} \quad F_{w,lat-} = \int_A v_t / (v_t < 0) dA \quad (Eq. 6')$$

$$F_{T,lat+} = \rho_0 C_p \int_A T v_t / (v_t > 0) dA \quad \text{and} \quad F_{T,lat-} = \rho_0 C_p \int_A T v_t / (v_t < 0) dA \quad (Eq. 7')$$

250 
$$F_{S,lat+} = \rho_0 \int_A S v_t / (v_t > 0) dA \quad \text{and} \quad F_{S,lat-} = \rho_0 \int_A S v_t / (v_t < 0) dA \quad (Eq. 8')$$

### 2.2.3 River fluxes

The river water volume flux  $F_{w,riv}$  is calculated as the sum over all the rivers of the product of the velocity of river flow at the river mouth,  $v_{riv}$ :

$$F_{w,riv} = \sum_{rivers} \int_A v_{riv} dA \quad (Eq. 9)$$

255 where  $A$  is the area of the river mouth section from the surface to the bottom.

The river heat flux  $F_{T,riv}$ , in PW, is computed from:

$$F_{T,riv} = \sum_{rivers} \rho_0 C_p \int_A T v_{riv} dA \quad (Eq. 10)$$

where  $T$  is the temperature (in °C) at the river mouth.

### 2.2.4 Atmospheric (surface) fluxes

260 The atmospheric freshwater volume flux is computed in Sv ( $1 \text{ Sv} = 10^6 \text{ m}^3 \text{ s}^{-1}$ ) from:

$$F_{w,surf} = \int_{Surf} (P - E) dx dy \quad (Eq. 11)$$

where P stands for the precipitation in  $m s^{-1}$ , E the evaporation in  $m s^{-1}$ , Surf is the SCS area limited by the six interocean straits shown in Fig. 1a.

265 The net surface heat flux ( $F_{T,surf}$ ), in PW, is the sum over the SCS of the short-wave radiation flux ( $F_{SR}$ ), long-wave radiation flux ( $F_{LR}$ ), sensible heat flux ( $F_{SEN}$ ) and latent heat flux ( $F_{LATENT}$ ):

$$F_{T,surf} = \int_{Surf} (F_{SR} + F_{LR} + F_{SEN} + F_{LATENT}) dx dy \quad (Eq. 12)$$

270 Finally, it should be noted that the flux calculations are numerically consistent with those carried out by the model through the advection scheme and its surface and continental boundary conditions. Along these lines,  $C_p$  and  $\rho_0$  constants correspond to the values used by the bulk formulas and the horizontal fluxes are calculated in the same way as in the advection scheme of the model. This allows to produce a strictly closed budget: the sum of all fluxes explains 100% of the variations of the water volume and of the total heat and salt contents at each time step of the simulation, as will be shown in Section 3.

## 2.3 Observational datasets

275 Satellite and tide gauges data are used for evaluating the representation of ocean surface characteristics (temperature, salinity, elevation). In-situ data are used to evaluate the surface and vertical representation of water mass properties and the mixed layer depth (MLD).

### 2.3.1 Satellite data

280 To evaluate the modeled SST (sea surface temperature), we use daily OSTIA (Operational Sea Surface Temperature and Sea Ice Analysis) outputs for the period 2010 – 2018, available at <https://data.nodc.noaa.gov/ghrsst/L4/GLOB/UKMO/OSTIA/> (last access 18 May 2023). OSTIA is a GHRSSST (Group for High Resolution Sea Surface Temperature) Level 4 SST daily product built from multiple spatial sensors and drifting and moored buoys data, with a horizontal resolution of  $1/18^\circ$ .

285 Regarding the SSS (sea surface salinity), we use outputs from the 9-day-averaged de-biased SMOS (Soil Moisture and Ocean Salinity) SSS Level 3 version 3, developed by Boutin et al. (2016). It has a resolution of 25 km and is available for the period 2010 – 2017. Data are distributed by the CECOS (Ocean Salinity Expertise Center) and the CNES - IFREMER CATDS (Centre Aval de Traitement des Données SMOS) via:

[https://data.catds.fr/cecos-locean/Ocean\\_products/L3\\_DEBIAS\\_LOCEAN/](https://data.catds.fr/cecos-locean/Ocean_products/L3_DEBIAS_LOCEAN/) (last access 18 May 2023).

To evaluate the SLA (sea level anomaly) and surface geostrophic currents, we use daily 1/4° global ocean gridded L4 sea surface heights in delayed – time of CMEMS, available at:

290 [https://data.marine.copernicus.eu/product/SEALEVEL\\_GLO\\_PHY\\_L4\\_MY\\_008\\_047/description](https://data.marine.copernicus.eu/product/SEALEVEL_GLO_PHY_L4_MY_008_047/description) (last access 18 May 2023). This altimetry product (hereafter called ALTI) is generated using data from different altimeter missions and covers the period from 1993 up to present (Ablain et al. 2015; Ray and Zaron, 2016). For model-data comparison, we extracted the daily altimetric SLA on the period of comparison and removed at each point of each dataset (model and altimetry) the temporal average over the same period.

### 295 **2.3.2 In-situ data**

More than 12000 Argo profiles were collected in the SCS between 2010 and 2018 (see Fig. 1b), available from [https://data-argo.ifremer.fr/geo/pacific\\_ocean/](https://data-argo.ifremer.fr/geo/pacific_ocean/) (<http://doi.org/10.17882/42182>, last access 18 May 2023).

The ALIS R/V crossed the SCS from 10 May to 28 July 2014 (see Fig. 1b), measuring SST and SSS every 6 s by the vessel-mounted Seabird SBE21 thermosalinometer (hereafter called TSG-Alis data).

300 Under the framework of a cooperative Vietnam - US international research program (Rogowski et al. 2019), a Seaglider sg206 was deployed on 22 January 2017 until 16 May 2017 in the SCS (see Fig. 1b). It collected 555 vertical profiles of conductivity, temperature and pressure from an unpumped Sea-Bird Electronics CTD (SBE 41CP). Conductivity, temperature and depth were sampled at 5 s intervals in the upper 150 m, corresponding to a resolution finer than 1 m, and between 55 – 100 s below. All sensors were factory calibrated. Salinity was corrected for the  
305 thermal lag error using a variable flow rate (Garau et al. 2011).

Argo, TS-Alis and glider in-situ measurements are compared in Section 4 with modeled profiles at the nearest point (in position and time).

The third version of GESLA (Global Extreme Sea Level Analysis) dataset, released in 2021, consists of 5119 tidal records obtained from multiple sources around the world (Haigh et al. 2023). This quasi-global, higher-frequency tide  
310 gauges dataset can be obtained from <https://www.gesla.org> (last access September 2023). Tide gauges records from 46 stations are collected over the SCS region, then compared with modeled tidal outputs at the nearest point.

### **2.4. Other global and regional models**

Besides the observational dataset, four widely used model outputs (COPERNICUS, INDES0, OFES and GLORYS, see Table 1) are collected and compared with our SYMPHONIE simulation over the same geographic zone (0.6-24°N,  
315 99-124°E) from 2010 to 2016, the common simulation period of all models.

**Table 1: Global and regional models used for the comparison with SYMPHONIE outputs.**

Model	SYMPHONIE	Global Ocean Physics Analysis and Forecast, called COPERNICUS here	CMEMS global ocean eddy-resolving reanalysis GLORYS12v1, called GLORYS here	Infrastructure Development of Space Oceanography, called INDESO here	OFES (OGCM for the Earth Simulator) simulation from JAMSTEC (Japan Agency for Marine-Earth Science and Technology) ver 2., called OFES here
Periods of simulation	2010-2018	1993-now	1993 - 2020	2009-2016	1958-2016
Spatial resolution	4 km ~ 1/28°	1/12°	1/12°	1/12°	1/10°
Number of vertical layers	50	50	50	50	105
Simulation zone	Regional 99°E - 124°E, 0.6°S - 24°N	Global	Global	Regional 90°E - 144°E, 20°S - 25°N	quasi-global
Assimilation	No	Yes	Yes	No	No
Tide included	Yes	No	No	Yes	Yes
References		Global Analysis Forecast Phy_001_024 Global Ocean 1/12° physics analysis and forecast provided by Copernicus Marine Environment, Monitoring Service (CMEMS) ( <a href="http://marine.copernicus.eu">http://marine.copernicus.eu</a> , last access August 2023), <a href="https://doi.org/10.48670/moi-00016">https://doi.org/10.48670/moi-00016</a>	<a href="https://data.marine.copernicus.eu/product/GLOBAL_MULTYEAR_PHY_001_030/description">https://data.marine.copernicus.eu/product/GLOBAL_MULTYEAR_PHY_001_030/description</a> , last access August 2023 <a href="https://doi.org/10.48670/moi-00021">https://doi.org/10.48670/moi-00021</a> ,	Tranchant et al. 2016	Sasaki et al. 2020 <a href="https://www.jamstec.go.jp/ofes/ofes2.html">https://www.jamstec.go.jp/ofes/ofes2.html</a> , last access August 2023 <a href="https://doi.org/10.17596/0002029">https://doi.org/10.17596/0002029</a>

## 2.5. Statistical evaluation

The simulated dataset  $S$  and observational dataset  $O$  (of the same size  $N$ ) are compared using three statistical parameters: the bias, the Normalized Root Mean Square Error (NRMSE) and the Pearson correlation coefficient  $R$ :

$$320 \quad Bias = \bar{S} - \bar{O} \quad (Eq. 13)$$

$$NRMSE = \frac{\sqrt{\frac{1}{N} \sum_{i=1}^N (S_i - O_i)^2}}{(O_{max} - O_{min})} \quad (Eq. 14)$$

$$R = \frac{\sum_{i=1}^N (O_i - \bar{O})(S_i - \bar{S})}{\sqrt{\sum_{i=1}^N (O_i - \bar{O})^2 \sum_{i=1}^N (S_i - \bar{S})^2}} \quad (Eq. 15)$$

Where  $S_i$  and  $O_i$  are respectively the simulated and observed series, and  $\bar{S}$  and  $\bar{O}$  their mean values. In Section 3, we use the same statistical evaluation methods for the comparison between online and offline computation of lateral oceanic fluxes:  $S_i$ ,  $O_i$ ,  $\bar{S}$  and  $\bar{O}$  are respectively replaced by  $OF_i$  (the offline fluxes series),  $ON_i$  (the online fluxes series),  $\overline{OF}$  and  $\overline{ON}$  (the corresponding mean values).

325

## 3. Added-value of the online budget computation

Computing online all the terms of the budget allows to calculate the exact net lateral fluxes through each lateral ocean boundary, hence to rigorously close the budgets at all time scales, but also to calculate the exact outflowing/inflowing fluxes at each time step. Computing the lateral term offline, using the modeled velocity, temperature and salinity at the output frequency, indeed relies on the assumption that the integral over the output period of the product of velocity and temperature (or salinity) is equal to the product of their integrals, thus that the turbulent term  $\overline{u'T'}$  in the following equation is negligible:

330

$$\overline{uT} = \overline{(\bar{u} + u')(\bar{T} + T')} = \overline{\bar{u}\bar{T}} + \overline{u'\bar{T}} + \overline{\bar{T}u'} + \overline{u'T'} = \bar{u}\bar{T} + \overline{u'T'} \quad (Eq. 16)$$

where  $u$  is the velocity normal to the vertical section and  $T$  the temperature at this point, and the overbar stands for the integral over the output period.

Here we quantitatively show the added value of the online computation of water volume, heat and salt budgets compared to the offline computation. In Fig. 2a,b,c we show each term of the budget equation for the interannual variations of water volume, heat and salt contents over the SCS, computed online and offline: annual variation, atmospheric surface fluxes, river fluxes, lateral oceanic fluxes and the sum of all fluxes, that should equal the annual variation as explained in Section 2.2. Table 2 provides the values of net, inflowing and outflowing annual fluxes computed online, and the bias, correlation and NRMSE between the offline and online computations.

340

First, those figures confirm that when computed online, the sum of annual fluxes is equal to the annual variation, i.e., that the budget equation is closed in our model. This is shown here for the interannual variations but is also verified at each time step of the whole simulation (figure not shown). Second, Fig. 2a,b,c quantitatively highlights the error

345

induced when neglecting the turbulent term in Eq. 16 by computing the lateral net fluxes offline. For the water volume flux, using the online (blue) and offline (cyan) computation for net lateral oceanic fluxes is equivalent since it does not imply any non-linear assumption. For the heat and salt fluxes however, the difference is significant: we obtain NRMSE of, respectively, 34% and 8% between the online and offline computations for, respectively, heat and salt net lateral fluxes over the SCS for the 2010-2018 period (Table 2).

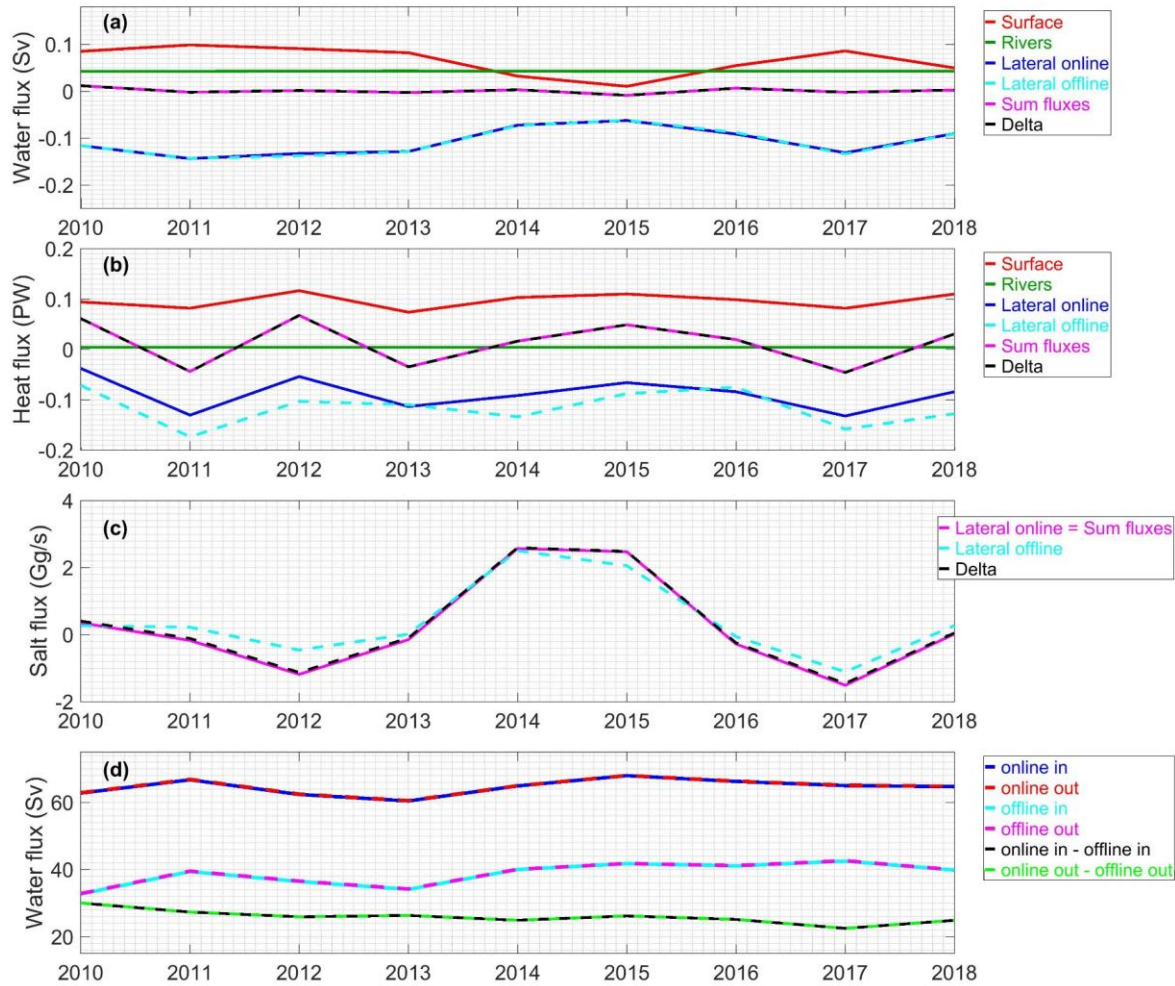


**Figure 2 : Atmospheric (surface, red), river (green) and net lateral oceanic (blue online, cyan offline) annual fluxes of (a) water volume (Sv), (b) heat (PW) and (c) salt ( $Gg.s^{-1}$ ) and their sum (magenta), and annual variations of water volume, heat and salt contents (black) over the period 2010 - 2018; (d) Annual lateral oceanic inflow (blue online, cyan offline) and outflow (red online, magenta offline) of water volumes (in absolute values) computed online and offline, and the difference online - offline (black for inflow, green for outflow).**

Third, the online computation allows us to compute separately the outflowing and inflowing terms of the lateral flux at each time step. Fig. 2d shows the annual water volume lateral inflowing and outflowing fluxes (in absolute values)

360 computed online and offline. Using the offline computational methods leads to important errors: the offline  
 computation underestimates the water volume outflow and inflow by a factor of ~2 (Table 2). Correlations of online  
 and offline water volume, heat and salt annual inflows or outflows are statistically significant (~ 0.80, p-value <0.01),  
 showing a similar chronology in both methods. However, the bias between online and offline inflowing or outflowing  
 lateral water volume, heat and salt fluxes is ~40% compared to the mean value, and high NRMSE values (~330%,  
 210% and 315% for water volume, heat and salt respectively, Table 2) are obtained. These results quantitatively  
 365 demonstrate the significant errors made when computing those fluxes offline and show the relevance of the online  
 computation.

**Table 2: Mean values over 2010-2018 of water volume, heat and salt net, inflowing and outflowing annual fluxes through the SCS computed online (1st column), and absolute (2nd) and relative (3rd) bias, correlation (4th) and NRMSE (5th) between online and offline computations.**

Lateral flux	Mean value in online computation	Bias (offline - online)	Bias/mean (relative bias) in %	Correlation (offline/online)	NRMSE in %
Water <b>volume</b> net (Sv)	<b>-0.108</b>	<b>-5E-4</b>	<b>0.46</b>	<b>1.00 (p=0.00)</b>	<b>2.44</b>
Heat net (PW)	<b>-0.088</b>	<b>-0.028</b>	<b>31.3</b>	<b>0.81(p&lt;0.01)</b>	<b>34.1</b>
Salt net (Gg/s)	<b>0.236</b>	<b>0.176</b>	<b>74.6</b>	<b>0.99 (p=0.00)</b>	<b>8.35</b>
Water <b>volume</b> in (Sv)	<b>64.6</b>	<b>-25.9</b>	<b>40.1</b>	<b>0.81 (p&lt;0.01)</b>	<b>327</b>
Water <b>volume</b> out (Sv)	<b>-64.7</b>	<b>25.9</b>	<b>40.1</b>	<b>0.81 (p=0.01)</b>	<b>330</b>
Heat in (PW)	<b>3.34</b>	<b>-1.29</b>	<b>38.6</b>	<b>0.82 (p&lt;0.01)</b>	<b>205</b>
Heat out (PW)	<b>-3.42</b>	<b>1.23</b>	<b>36.0</b>	<b>0.85 (p&lt;0.01)</b>	<b>213</b>
Salt in (Gg/s)	<b>2285</b>	<b>-914</b>	<b>40.0</b>	<b>0.82 (p&lt;0.01)</b>	<b>313</b>
Salt out (Gg/s)	<b>-2285</b>	<b>914</b>	<b>40.0</b>	<b>0.82 (p&lt;0.01)</b>	<b>316</b>

#### 370 4. Model performance in representing sea surface and water masses characteristics

In this section, we evaluate the ability of the simulation to simulate over 2010-2018 the characteristics of SCS sea surface (temperature, salinity, sea surface elevation including tides), water masses and mixed layer depth.

##### 4.1 Sea surface characteristics

375 We evaluate here the ability of the model to represent sea surface characteristics and their variability at the tidal, seasonal and interannual scale by comparing them with tide gauges data, tide reanalysis and satellite observations of sea surface temperature, salinity and elevation.

#### 4.1.1 Tides

The tide representation over the coastal zone is evaluated by comparing numerical results with the 46 GESLA tide gauges data available over the SCS. Results are presented in Fig. 3. We obtain similar simulated and observed values  
380 in amplitudes and phases with relatively weak biases for the four main tidal components (K1, O1, M2 and S2). The SCS is indeed one of the few regions of the global ocean where diurnal tides (K1, O1) dominate semi-diurnal tides (M2, S2) (Guohong, 1986). The model overestimates diurnal tides amplitude by ~ 15 cm in the southern Gulf of Thailand for K1 and underestimates it by ~10 cm in the Gulf of Tonkin and Sulu Sea coastal zone for O1 (Fig. 3c1,c2). Concerning the semi-diurnal tide, amplitude differences are about  $\pm 5$  cm for most of stations, the strongest biases are  
385 observed at the Sulu Sea (~20 cm for M2 and ~10 cm for S2) and Celebes Sea (~ -20 cm for M2 and S2) (Fig. 3c3,c4).



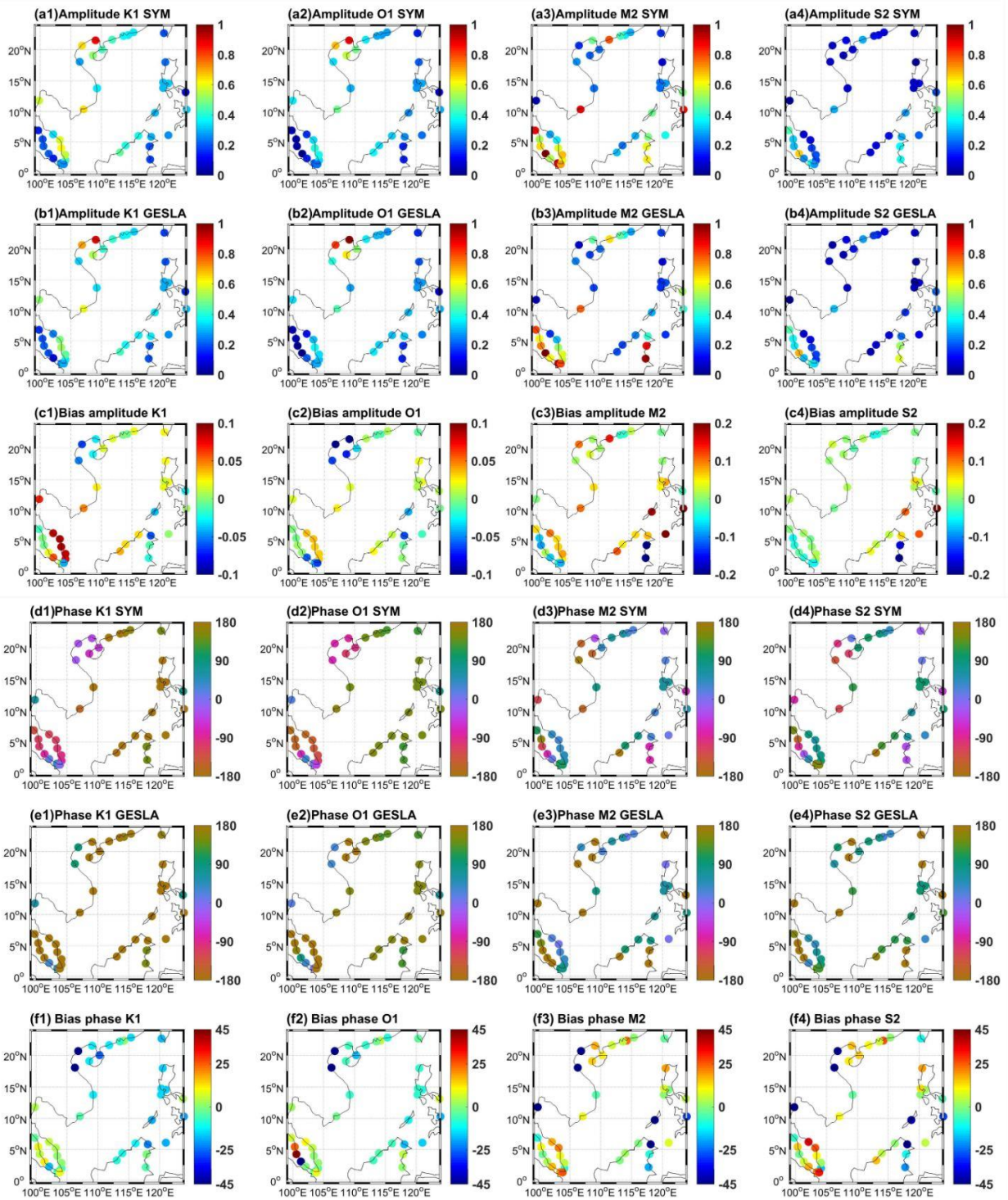
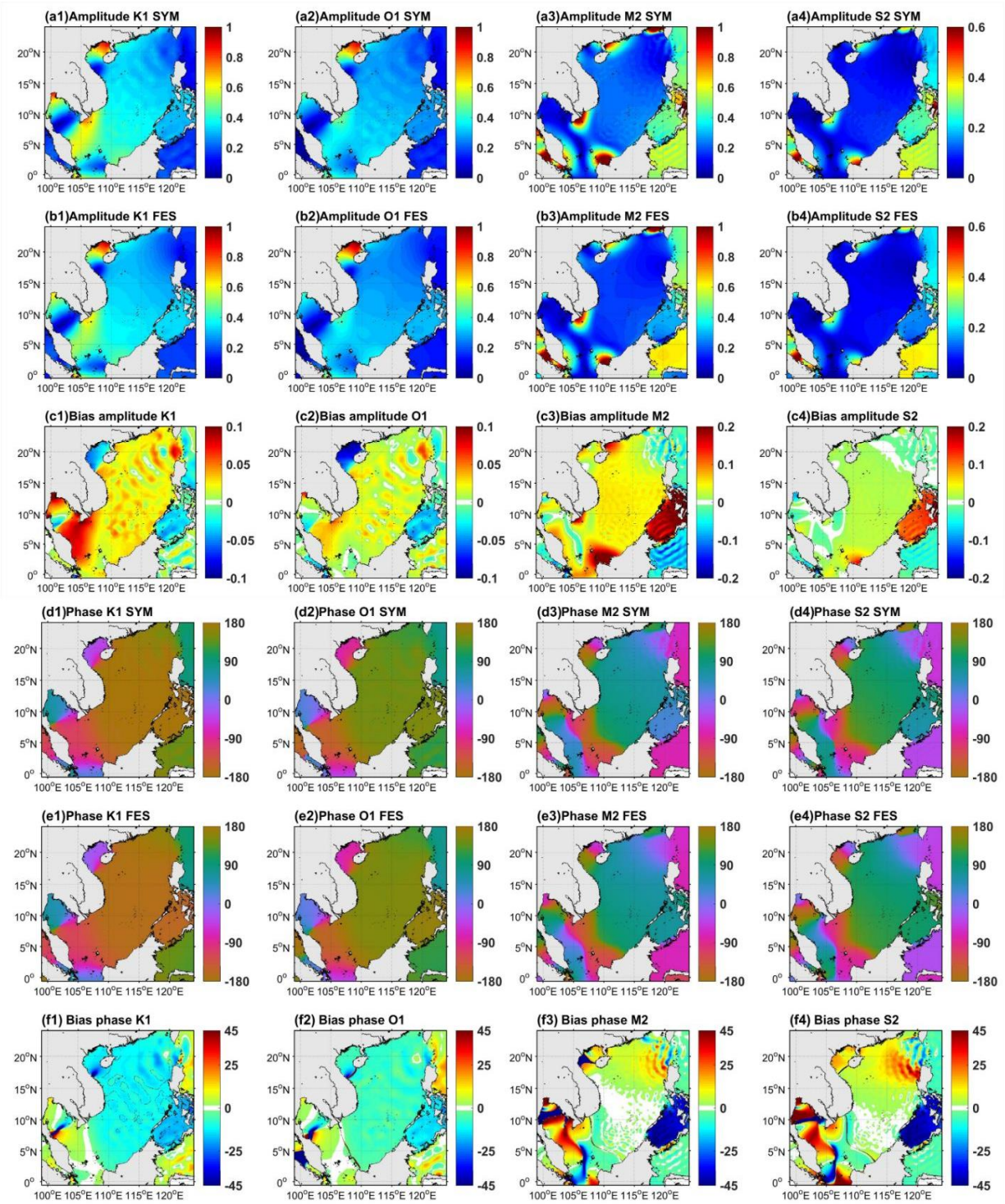


Figure 3 : Amplitude (m) and phase (degree) of four tidal components K1, O1, M2, S2 in the model (SYM, a1-a4, d1-d4) and GESLA tide gauge dataset (b1-b4, e1-e4) and model bias compared to GESLA (c1-c4, f1-f4)

390 FES2014b is used to provide the tidal forcing at the lateral boundaries of our numerical domain, located outside the  
SCS (Fig. 1a). FES2014b assimilates satellite and in-situ sea surface elevation data, allowing it to be very close to  
observations, as shown by Piton et al. (2020) over the Gulf of Tonkin. We therefore also use it, complementary to  
GESLA tide gauges data, to evaluate the tidal solution produced by our model over the inner open sea domain. We  
show in Fig. 4 the observed and simulated tidal amplitude and phase for K1, O1, M2 and S2, the four principal tidal  
395 components in the SCS region. The spatial distribution of tidal constituents obtained from the model and from  
FES2014b is similar to the study of Phan et al. (2019). Diurnal tides prevail over the Gulf of Tonkin, the Gulf of  
Thailand and the southwestern SCS. Mixed tides (mainly semi-diurnal tides) prevail along southern China, the  
northwest coast of Borneo and the continental shelf of the Mekong delta. For those four tidal components, we obtain  
a strong similarity both for amplitudes and phases between the model and FES2014b over most of the modeled domain.  
400 As observed from the comparison with tide gauges, the most noticeable weaknesses are a small ( $< 10$  cm)  
underestimation of diurnal (K1 and O1) amplitude in the Sulu Sea and Gulf of Tonkin, an overestimation ( $\sim 20$  cm) of  
semi-diurnal (M2 and S2) amplitude in the Sulu Sea, and a small overestimation of K1 amplitude off the Mekong  
Delta. The bias of semi-diurnal tidal amplitudes in the Sulu Sea may be related to the prescribed bathymetry in the  
area, with many small islands separating this area from the surrounding seas. Comparing our results with FES2014b  
405 tidal solution and tide gauge data therefore shows that SYMPHONIE reproduces realistically the tidal solution in the  
SCS, both in the open sea and in the coastal area.

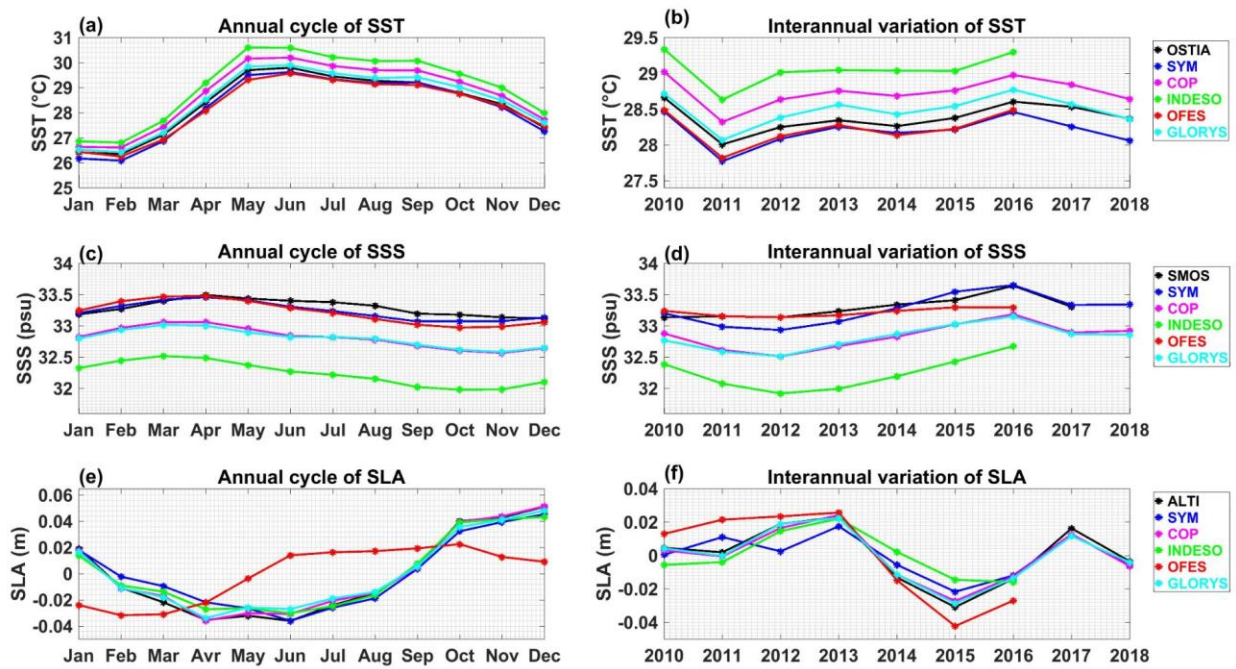




**Figure 4: Amplitude (m) and phase (degree) of four tidal components K1, O1, M2, S2 in the model (SYM, a1-a4, d1-d4) and the global tidal product FES2014b (FES, b1-b4, e1-e4) and the bias in the model compared to FES2014b (c1-c4, f1-f4).**

410 **4.1.2 Seasonal cycle of sea surface temperature, salinity and elevation**

We show in Fig. 5 the seasonal cycle (Fig. 5a,c,e) and the interannual variations (Fig. 5b,d,f) of SST, SSS and SLA computed from model outputs (for SYMPHONIE as well as COPERNICUS, INDESO, GLORYS and OFES) and from the corresponding satellite observations. Table 3 shows the corresponding bias, NRMSE and correlation coefficients.



415 **Figure 5 : Time series of climatological monthly mean (left, computed over 2010-2016, the period common to all models) and yearly mean (right, over 2010-2018 except for OFES and INDESO, available only until 2016) of SST (°C, a, b), SSS (psu, c, d) and SLA (m, e, f) averaged over the SCS domain, computed from different models (SYM, blue; COPERNICUS, magenta; INDESO, green; OFES, red; GLORYS, cyan) and from satellite observations (OSTIA, SMOS and ALTI, black).**

420 The annual cycle of SST averaged over the SCS (Fig. 5a) is very well simulated, with a highly significant correlation ( $R=0.99$  and  $p$ -value  $p < 0.01$ , corresponding to a significant level higher than 99%) and a small NRMSE (5.7%) between SYMPHONIE outputs and OSTIA, and a slight bias of  $-0.18$  °C for the period 2010 - 2018. In all datasets, the monthly climatological cycle of SST reaches its maximum value in May/June (spring-summer) and decreases to its minimum in January/February (winter). This monthly climatological SST agrees with the study of Kumar et al.

425 (2010), who observed the same SST annual cycle by analyzing hydrographic WOA data (World Ocean Atlas, 2005).

SYMPHONIE SSS seasonal cycle (Fig. 5c) also shows a good agreement with SMOS data, with a highly significant correlation of 0.91 ( $p < 0.01$ ), a low NRMSE equal to 19%, and a slight negative bias ( $-0.04$  psu). In both model and data, the average SSS is maximum in April (spring) with values of 33.47 psu in the model and 33.52 psu in SMOS, and minimum from September to December (autumn) with 33.07 psu in the model and 33.17 psu in SMOS. This

430 significant seasonal variation of SSS in the SCS, with high salinity in winter-spring and low salinity in summer-  
autumn was also obtained by Kumar et al. (2010) and Zeng et al. (2014).

The annual cycle of SLA obtained with the model and ALTI data during the period 2010 - 2018 shows a minimum  
value in spring-summer (June) with -0.033 m both for SYMPHONIE and ALTI (Fig. 5e). The SLA reaches its highest  
value in winter (December) with 0.039 m and 0.049 m respectively for the model and ALTI. The model outputs and  
435 the altimeter measurements have a highly significant correlation ( $R=0.97$ ,  $p<0.01$ ), and a small NRMSE value (10%).  
The simulated monthly climatological SLA is also in agreement with Shaw et al. (1999) and Ho et al. (2000): using  
TOPEX/Poseidon altimeter data, they both concluded on a higher SLA in winter and lower SLA in summer over the  
SCS.

We then show the simulated and observed maps of SST, SSS and SLA climatologically averaged over the boreal  
440 winter (December, January and February, DJF) and summer (June, July and August, JJA) for SYMPHONIE (Fig. 6)  
as well as the corresponding bias for the 5 models (Fig. 7).

In both winter and summer, SYMPHONIE SST is very close to observations, with highly significant spatial correlation  
(respectively  $R=0.99$  and  $0.84$  in winter and summer,  $p<0.01$ ) and similar ranges compared to OSTIA (Fig. 6a,b). In  
winter, the model shows an average negative bias of  $-0.28$  °C, and colder zones offshore southern Vietnam and in the  
445 northern basin. In summer (Fig. 6c,d), the average negative bias is reduced to  $-0.17$  °C, and the simulation produces a  
SST colder than OSTIA in the northern SCS near Taiwan, off southern Vietnam coast, along the Mekong delta, and  
in the Sulu and Celebes seas (see Fig. 1a). On the other hand, simulated SST is warmer in the Gulf of Tonkin, Gulf of  
Thailand and the southern basin.

SYMPHONIE spatial distribution of SSS also shows a highly significant spatial correlation with SMOS for both  
450 seasons ( $R=0.88$  and  $0.84$  psu in winter and summer, respectively,  $p<0.01$ ). The model has a positive bias in winter  
( $0.05$  psu), and a negative bias in summer ( $-0.1$  psu). In winter (Fig. 6e,f), the Chinese and Vietnam coastal zones and  
the Gulf of Thailand are fresher in the model than in SMOS data, whereas the center of the basin and the southern  
Gulf of Tonkin are saltier. In summer (Fig. 6g,h), we obtain a significantly lower SSS at the big river mouths (Pearl  
River, Red River, Mekong River), in the Gulf of Thailand and in the Malacca Strait in model outputs compared to  
455 SMOS. SMOS, with a resolution of 25 km, might however not be able to capture these salinity changes in the coastal  
zone.

Both in winter and summer, the simulated and observed seasonal mean spatial distributions of SLA show a highly  
significant correlation ( $R=0.97$ ,  $p<0.01$ , Fig. 6i,j,k,l). SYMPHONIE shows very weak negative seasonal biases in SLA  
compared to ALTI ( $-0.008$  m in winter and  $-0.003$  m in summer). In the Gulf of Thailand, the simulated SLA is lower  
460 in winter and higher in summer compared to ALTI. Regarding the geostrophic currents, we obtain great similarities  
between the model and ALTI. In winter when the northeastern monsoon dominates, two cells of cyclonic gyre cover  
the whole basin, one near Luzon and another at the Sunda shelf. In summer, with the southwest monsoon, most of the  
SCS geostrophic currents reverse and flow northeast. The geostrophic currents are most intense at the Sunda shelf

zone (see Fig. 1a) in winter. In summer, we observe strong geostrophic flows at the southern Vietnam coast, and at  
465 the east of the Malaysian coast. The intensity and direction of those seasonal geostrophic currents are consistent with  
previous studies (e.g., Da et al. 2019; Wang et al. 2006b).

Last, Fig. 8i,j shows the observed TSG-Alis SST and SSS during spring-summer 2014 and the corresponding  
colocalized simulated SSS and SST. Again, SYMPHONIE shows a strong similarity with TSG-Alis data, with  
correlation coefficients of 0.70 and 0.82 ( $p < 0.01$ ), for SST and SSS respectively, during this 6th year of the simulation.

470 **Table 3 : Bias, correlation coefficients and NRMSE values (for the climatological monthly annual cycle and interannual yearly time series (in italics) shown in Fig. 5) for the SST, SSS and SLA simulated by SYMPHONIE, OFES, INDESO, COPERNICUS and GLORYS compared to satellite observations (OSTIA, SMOS and ALTI, respectively), and for the climatological monthly annual cycle of simulated MLD shown in Fig. 9 compared to Argo data. The period over which indicators are computed is indicated below the model name**

Models and period		SYMPHONIE 2010-2018	SYMPHONIE 2010-2016	OFES 2010-2016	INDESO 2010- 2016	COPERNICUS 2010-2016	GLORYS 2010- 2016
Bias (m)	SST (°C)	-0.18	-0.16	-0.14	0.70	0.38	0.14
	SSS (psu)	-0.04	-0.05	-0.07	-1.05	-0.48	0.14
	SLA (m)	-4.5E-4	1.2E-3	1.3E-3	1.2E-3	1.2E-3	1.3E-3
	MLD (m)	9.4	9.29	7.13	15.4	15.3	10.5
Correlation coefficient R (%)  annual cycle/ interannual	SST	0.99 <i>p&lt;0.01</i> <i>0.94</i> <i>p&lt;0.01</i>	0.99 <i>p&lt;0.01</i> <i>0.98</i> <i>p&lt;0.01</i>	0.99 <i>p&lt;0.01</i> <i>0.98</i> <i>p&lt;0.01</i>	0.99 <i>p&lt;0.01</i> <i>0.97</i> <i>p&lt;0.01</i>	0.99 <i>p&lt;0.01</i> <i>0.99</i> <i>p&lt;0.01</i>	0.99 <i>p&lt;0.01</i> <i>0.97</i> <i>p&lt;0.01</i>
	SSS	0.91 <i>p&lt;0.01</i> <i>0.91</i> <i>p&lt;0.01</i>	0.86 <i>p&lt;0.01</i> <i>0.91</i> <i>p&lt;0.01</i>	0.80 <i>p&lt;0.01</i> <i>0.78</i> <i>p=0.04</i>	0.72 <i>p&lt;0.01</i> <i>0.78</i> <i>p=0.04</i>	0.83 <i>p&lt;0.01</i> <i>0.86</i> <i>p=0.01</i>	0.83 <i>p&lt;0.01</i> <i>0.92</i> <i>p&lt;0.01</i>
	SLA	0.97 <i>p&lt;0.01</i> <i>0.90</i> <i>p&lt;0.01</i>	0.98 <i>p&lt;0.01</i> <i>0.89</i> <i>p&lt;0.01</i>	0.31 <i>p=0.3</i> <i>0.95</i> <i>p&lt;0.01</i>	0.99 <i>p&lt;0.01</i> <i>0.85</i> <i>p=0.01</i>	0.99 <i>p&lt;0.01</i> <i>0.99</i> <i>p&lt;0.01</i>	0.99 <i>p&lt;0.01</i> <i>0.99</i> <i>p&lt;0.01</i>
	MLD	0.98 <i>p&lt;0.01</i>	0.98 <i>p&lt;0.01</i>	0.99 <i>p&lt;0.01</i>	0.97 <i>p&lt;0.01</i>	0.98 <i>p&lt;0.01</i>	0.99 <i>p&lt;0.01</i>
NRMSE (%)  annual cycle/ interannual	SST	5.73 26.2	5.15 24.8	5.40 21.5	20.7 107	11.2 58.0	4.27 22.8
	SSS	18.9 20.0	23.4 26.1	35.4 29.9	282 211	129 96.9	132 98.4
	SLA	9.92 17.5	7.85 16.5	35.9 19.6	5.74 18.1	2.77 4.59	4.71 3.45
	MLD	24.3	25.8	19.2	40.2	39.8	27.5



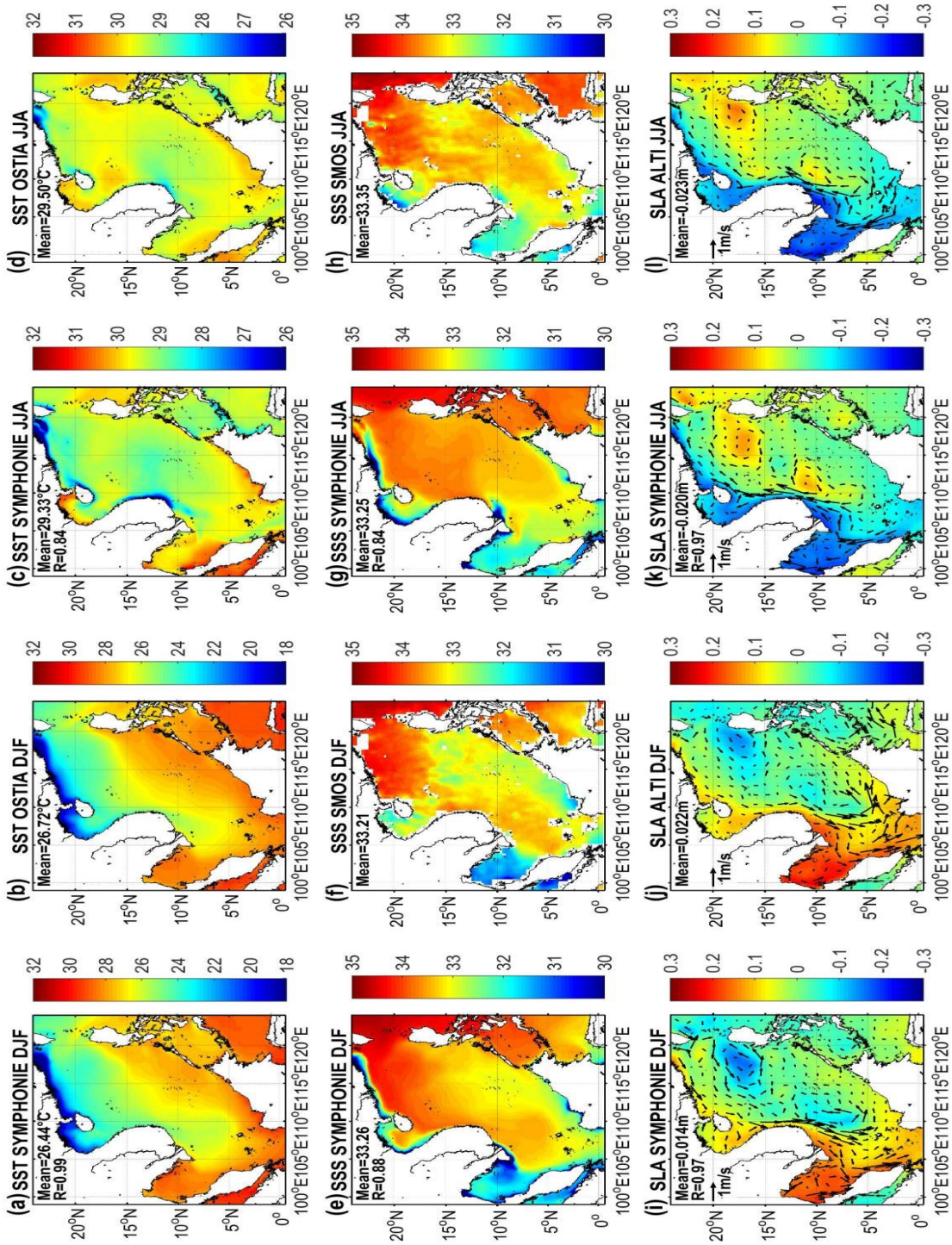


Figure 6 : Spatial distribution of winter (DJF) and summer (JJA) climatologically averaged SST (°C, a, b, c, d), SSS (psu, e, f, g, h), SLA (m) and geostrophic current (m/s, i, j, k, l) in model outputs and corresponding satellite observations over 2010-2018. R stands for the spatial correlation coefficient (here p-value is always smaller than 0.01)



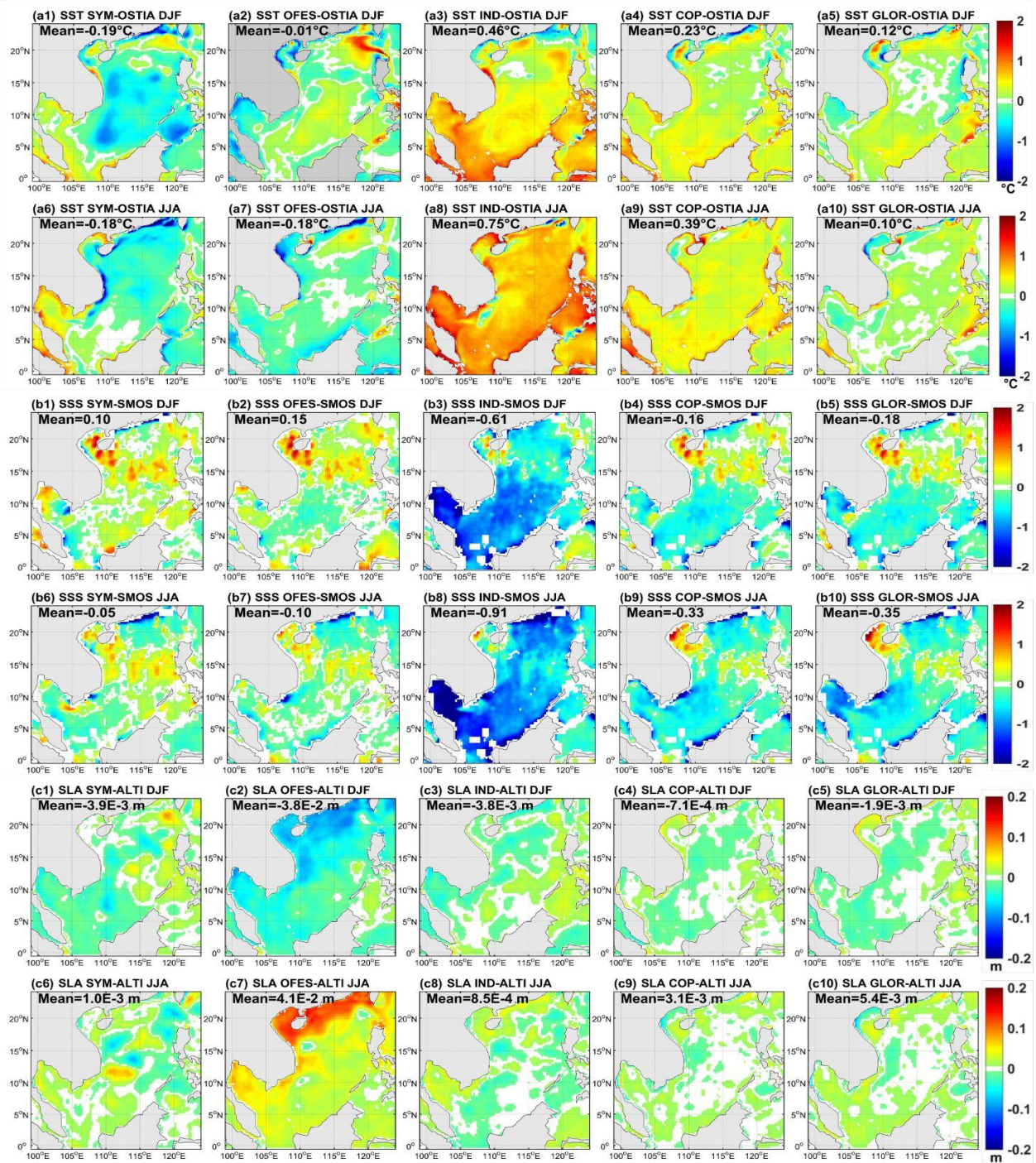


Figure 7: Maps of biases between models and satellite datasets averaged in winter (December, January, February, DJF) and summer (June, July, August, JJA) during the period 2010 - 2016 for SST (°C, compared to OSTIA, a1-a10), SSS (psu, compared to SMOS, b1-b10) and SLA (m, compared to ALTI, c1-c10).

### 4.1.3 Interannual variations of sea surface temperature, salinity and elevation

485 We obtain a highly significant correlation coefficient between SYMPHONIE and OSTIA ( $R=0.94$ ,  $p<0.01$ ) regarding yearly SST interannual variations (Fig. 5b). The yearly  $-0.18$  °C SST bias is nearly constant over the period and the NRMSE is 26%. From 2010 to 2018, the averaged yearly SST over the basin reaches its highest values in 2010 and 2016 ( $28.47^{\circ}\text{C}$  and  $28.46^{\circ}\text{C}$ , respectively). This is consistent with the study of Yu et al. (2019), who found a co-occurrence between those SST positive anomalies peaks and El-Niño events in 2009-2010 and 2015-2016 (see the  
490 NOAA ONI time series available at [https://origin.cpc.ncep.noaa.gov/products/analysis\\_monitoring/ensostuff/ONI\\_v5.php](https://origin.cpc.ncep.noaa.gov/products/analysis_monitoring/ensostuff/ONI_v5.php)). The minimum of averaged SST ( $27.77$  °C) occurs in 2011, corresponding to the 2011-2012 La Niña event. Yu et al. (2019) obtained the same interannual time-series by analyzing MODIS satellite-derived SST data for the period 2003 - 2017.

The simulated interannual variations of yearly SSS (Fig. 5d) show a highly significant correlation ( $R=0.91$ ,  $p<0.01$ ) and a rather low NRMSE value (20%) with satellite data. There is a significant increase of the annual averaged SSS  
495 over the SCS between 2012 to 2016, both in the model outputs and SMOS data. Over the period 2010 - 2017, the SSS reaches a low value in 2012 (32.93 psu for the model, 33.14 psu for SMOS), then increases continuously until a maximum value in 2016 (33.65 psu for the model, 33.64 psu for SMOS). The freshening until 2012 and strong salinification during the following four years are in agreement with observations of Zeng et al. (2014, 2018), who  
500 revealed that 2012 was the year with the lowest recorded value of SSS in the SCS over a 50-year period, and that the SSS then increased from late 2012 to 2016.

In terms of SLA interannual variations, our model and ALTI show strong similarities with a NRMSE equal to 17.5% (Fig. 5f) and a highly significant correlation ( $R=0.90$ ,  $p<0.01$ ). During the studied period, the overall averaged SLA is maximum in 2013 (0.017 m in model outputs and 0.023 m in ALTI), and minimum in 2015 ( $-0.02$  m in the model  
505 and  $-0.03$  m in ALTI).

### 4.1.4 Comparison with other models

SYMPHONIE performances in representing sea surface characteristics are also compared with other numerical dataset over 2010 - 2016, the period common to all simulations (Fig. 5 and 7 and Table 3). The most striking weaknesses are an overestimation of SST ( $0.7$  °C) and underestimation of SSS ( $-1.1$  psu) in INDESO and a wrong representation of  
510 SLA seasonal cycle in OFES (correlation of 0.31). Apart from this, all models compare well with observations in terms of bias, seasonal cycle and interannual variability, and spatial variability. Moreover, SYMPHONIE is always in the upper performance range, for bias, correlation coefficients and RMSE. In comparison with other models, SYMPHONIE thus shows a good performance in simulating the seasonal cycle and interannual of surface characteristics, and performs as well or even better than models that include assimilation (GLORYS and  
515 COPERNICUS).

Those comparisons of SYMPHONIE SST, SSS and SLA time series and spatial fields with observations dataset and other simulations available from models at coarser resolution therefore shows the added-value of our high-resolution simulation in realistically reproducing the annual cycle and interannual variations and the seasonal spatial distributions of SCS surface hydrological characteristics and circulation over the period 2010-2018.

## 520 4.2 Water masses characteristics

We hereafter examine the performance of SYMPHONIE in simulating the vertical distribution of water masses temperature and salinity properties. For that, we compare model results with Argo and glider observations. Fig. 8a-h show the colocalized simulated and observed temperature and salinity profiles, their mean value and the bias between model and data.

525 We obtain a strong agreement between the simulated and observed temperature and salinity profiles both for Argo floats (over the period 2009-2018) and glider (winter-spring 2016) outputs (Fig. 8a-h). In particular the maximum salinity observed in the intermediate water mass, corresponding to the Maximum Salinity Water (MSW), is well reproduced by SYMPHONIE. In general, modeled temperatures are lower than measured temperatures, with a negative bias in the whole water column (Fig. 8b,f). The highest biases are located in the subsurface layer (50-200 m),  
530 with maximum biases of  $-1.2^{\circ}\text{C}$  compared to Argo data and of  $-1.5^{\circ}\text{C}$  compared to glider data. Under 200 m, the temperature bias is stable, varying around  $0.2\text{-}0.5^{\circ}\text{C}$  compared to Argo floats, and  $0.7\text{-}1^{\circ}\text{C}$  compared to glider data. Model results show a general very low positive salinity bias compared to Argo and glider data below 200 m. A higher salinity bias is obtained in the subsurface layer:  $0.2$  psu compared to Argo data (Fig. 8d) and  $0.3$  psu compared to glider data (Fig. 8h). Therefore, our simulation accurately represents the various SCS water masses characteristics  
535 over the water column. It is moreover noteworthy that in 2016, i.e. the 7th year of simulation, those characteristics are reproduced without a significant drift.

SYMPHONIE also shows a good performance in reproducing the temperature and salinity vertical distribution in comparison with other numerical datasets. Temperature and salinity profiles averaged over the zone  $112\text{-}118^{\circ}\text{E}$ ,  $12\text{-}18^{\circ}\text{N}$  and the period 2010-2016 are shown in Fig. 9 a. COPERNICUS and GLORYS profiles are closest to Argo  
540 thanks to the assimilation. Concerning the models without assimilation, INDESO shows the lowest temperature bias (maximum  $0.4^{\circ}\text{C}$  at 100-150 m depth) compared to Argo. Higher temperature biases are observed with SYMPHONIE ( $\sim -1.5^{\circ}\text{C}$  at 50-100m depth) and OFES ( $\sim -0.7^{\circ}\text{C}$  at 800m). Regarding the salinity, SYMPHONIE shows the lowest bias for the upper 0-300 m layer ( $\sim 0\text{-}0.3$  psu), while INDESO shows a strong surface fresh bias (up to  $0.8$  psu) and OFES overestimates the salinity maximum (by  $\sim 0.5$  psu at 100-200 m depth). Underneath 200 m, all models present  
545 low salinity biases in comparison with observation and OFES shows the strongest bias ( $\sim -0.1$  psu at 500 m).

Argo floats, glider and model data show water masses characteristics in agreement with previous studies done on water masses over the SCS (Uu and Brankart, 1997; Penjan et al. 1997; Rojana-anawat et al. 1998; Saadon et al. 1998a, b) and the Pacific (Talley et al. 2011) (Fig. 8a-h). In the upper layer (0-50 m), we observe both the Open Sea

Water (OSW), characterized by salinities of 33-34 psu and temperatures of 25-30 °C, and the Continental Shelf Waters (CSW) with low salinities (< 33 psu) and temperatures between 20 and 30°C (depending on the season). The 50-100 m layer is characterized by the mixing between the Northern Open Sea Water (NOSW) and the Pacific Ocean Water (POW) during winter. The NOSW has salinities of 34-34.5 psu and temperatures of 23-25 °C. The POW is saltier with salinities of 34-35 psu and temperatures of 25-27 °C. Deeper, at 100-200 m, the MSW is characterized by temperatures between 15-17 °C and salinities between 34.5 psu and 35 psu and is a property of the equatorial regions (Rojana-anawat et al. 1998). Below the MSW, from 200-1000 m, the North Pacific Intermediate Water (NPIW) and Pacific Equatorial Water (PEW) are flowing with temperatures and salinities between 5-13 °C and 34-35 psu, respectively. The Deep Water (DW), below 1000 m, is identified by temperatures of 2-5 °C, and salinities of 34.3 - 34.7 psu. Temperature profiles located in the Sulu Sea do not follow those characteristics in the deep layers, both in Argo and model outputs, showing temperature varying from 7 to 10°C below 700 m. This marginal sea, nearly isothermal, indeed possesses unique water characteristics, with a potential temperature varying around 9.8°C below 1000 m (Wyrki, 1961; Chen et al. 2006; Gordon et al. 2011), much higher than those of neighboring seas such as the SCS, the Celebes Sea and the Western (Qu and Song, 2009).



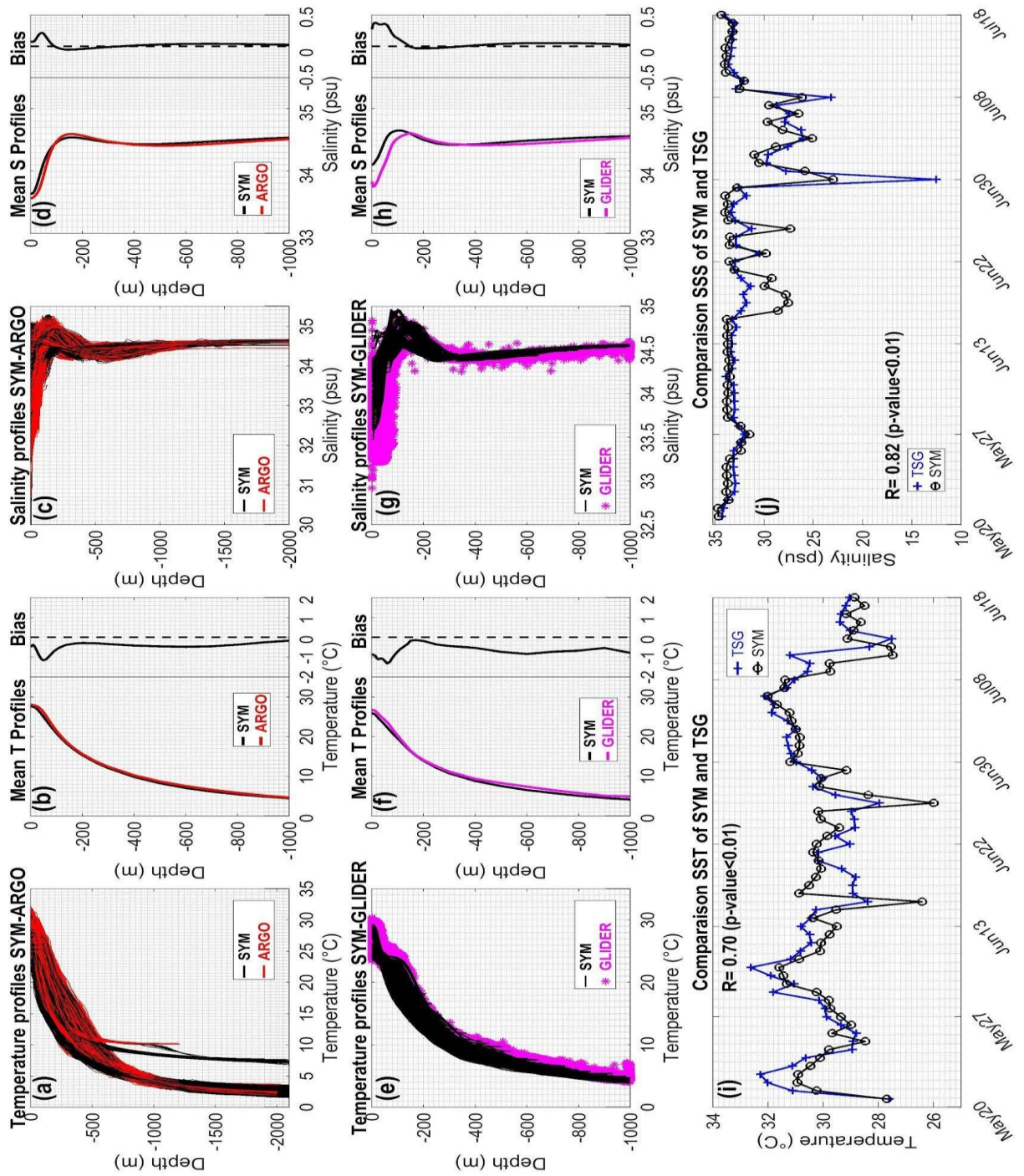


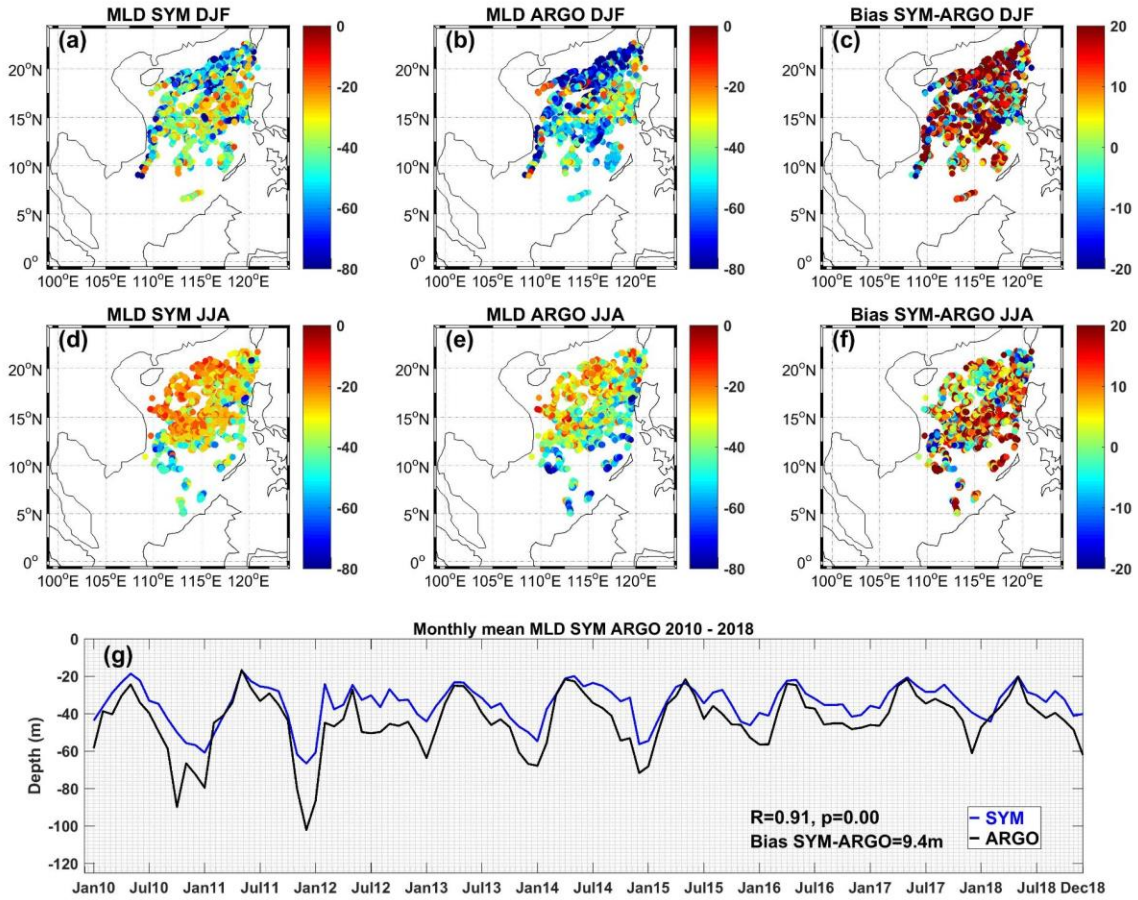
Figure 8 : Temperature (°C) and salinity (psu) vertical profiles (all profiles, mean profiles and mean bias between model and observations) from SYMPHONIE outputs (black) compared with Argo floats (a,b,c,d, red) and glider measurements (e,f,g,h, magenta). (i) SST (°C) and (j) SSS (psu) from SYMPHONIE (black) and TSG-Alis data (blue)

### 4.3 Mixed layer depth

The seasonal distribution of simulated mixed layer depth (MLD) in the SCS basin is evaluated by comparison with values computed from Argo profiles. The MLD is calculated based on a 0.5 °C temperature criteria, corresponding to the temperature difference between the near-surface and the MLD.

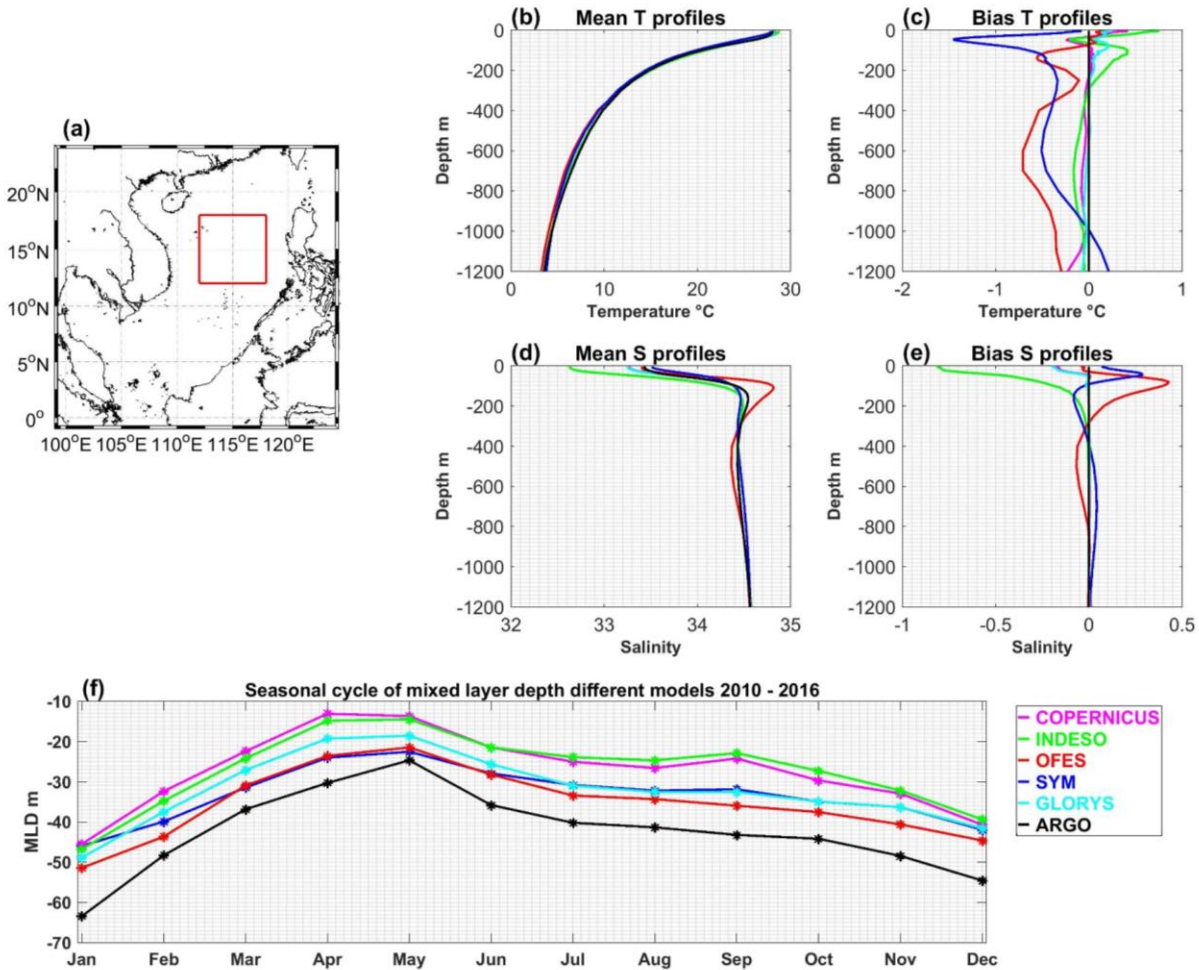
Figure 9 shows the winter (DJF) and summer (JJA) spatial distributions of the colocalized simulated and observed MLD at Argo locations (in space and time), as well as the simulated and observed time series of monthly mean MLD averaged over the Argo points over the SCS. Spatial distributions of SYMPHONIE MLD are close to observed values. Observed and simulated MLD are deeper in winter (varying between ~80 m in the north and ~30 m in the east, Fig. 9a,b) and shallower in summer (varying between ~50 m in the south and ~20 m in the north, Fig. 9d,e). The simulated MLD in both seasons are in general shallower than MLD obtained from Argo profiles, with bias locally reaching 20 m in DJF (Fig. 9c,f). This shallower MLD explains the slight temperature underestimation and salinity overestimation around ~50 m depth (Fig. 9b,d). The average bias over the area and 2010-2018 period is equal to 9.4 m (Fig. 9g), and is stronger for higher values of MLD in winter (e.g. ~-40 m in January 2012). This bias is stable over the 9 years of analysis (Fig. 9g), indicating that there is no drift in terms of simulated MLD. Moreover, the observed temporal variability of MLD is well reproduced by SYMPHONIE, with a 0.91 ( $p < 0.01$ ) highly significant correlation between the simulated and observed interannual timeseries of monthly MLD.

Fig. 10f illustrates the climatological seasonal cycle of MLD over the zone 112-118°E, 12-18°N and the period 2010-2016 for modeled outputs compared to Argo. All models underestimate the MLD (Table 3), but simulate similar annual evolution of MLD, with highly significant correlation between the simulated and observed climatological monthly timeseries ( $R \sim 0.98$ ,  $p < 0.01$ ). The deepest MLD is observed in winter and the shallowest in April-May. OFES shows the smallest underestimation and NRMSE (7.3 m, 19%), followed by SYMPHONIE (9.10 m, 25%). The strongest biases and NRMSE are obtained from INDES0 (15.6 m, 41%) and COPERNICUS (15.5 m, 40%). This systematic underestimation of simulated MLD, stronger for higher values of MLD, could be partly related to the underestimation of wind speed. Compared to QuikSCAT, ECMWF analysis (used to prescribe the atmospheric forcing to SYMPHONIE) indeed underestimates sea surface wind speed by  $\sim -1 \text{ m}\cdot\text{s}^{-1}$  on average over the region (see Fig. S1). More generally, regional atmospheric models underestimate sea surface wind speed over the region, especially for periods and areas of strong winds (Herrmann et al. 2020, 2022).



595 **Figure 9 : Seasonal distribution of MLD (m) from (a,d) SYMPHONIE and (b,e) Argo data and their bias (c,f) in winter (1st row) and summer (2nd row) over 2010-2018; (g) time series of monthly MLD (m) averaged over the domain in SYMPHONIE and Argo data.**





600 **Figure 10 :** (a) Comparison zone ( red box, 112-118°E, 12-18°N); Simulated (SYMPHONIE, COPERNICUS, INDESO, GLORYS and OFES) and observed (Argo) temperature (b, °C) and salinity (d, psu) profiles averaged over the comparison zone and 2010-2016 and their biases (c,e) compared to Argo; (f) Climatological monthly time series of simulated and observed mixed layer depth over the comparison zone and the period 2010 - 2016.

### 5. Evaluation and analysis of SCS interocean straits water volume exchanges and SCS water budget

605 In this part, we first compile the available estimates of fluxes through SCS interocean straits, and use them to assess the ability of our model to reproduce those fluxes. We then use the SYMPHONIE simulation to assess the contributions of lateral interocean, surface atmospheric and river fluxes and of internal variations to the SCS water volume budget at climatological and seasonal scales.



### 5.1 Evaluation of simulated water volume fluxes at interocean straits

610 A summary of lateral water volume transport published estimates at different SCS interocean straits is presented in  
 Table 4. In-situ measurements are more numerous for Luzon and Taiwan Straits than for Karimata and Mindoro, and  
 no direct measurements are available at Balabac and Malacca. Given the complexity of bathymetry and current  
 conditions in interocean straits, it is difficult to obtain accurate estimates of year-round transport from in-situ  
 observations. In addition to measurements, several models have thus been used to quantify those transports. For a  
 615 given strait, those studies provided various results, due to differences in methodology (sampling, studied period,  
 choice of transects, model configuration, resolution, parameterisations and forcings...).

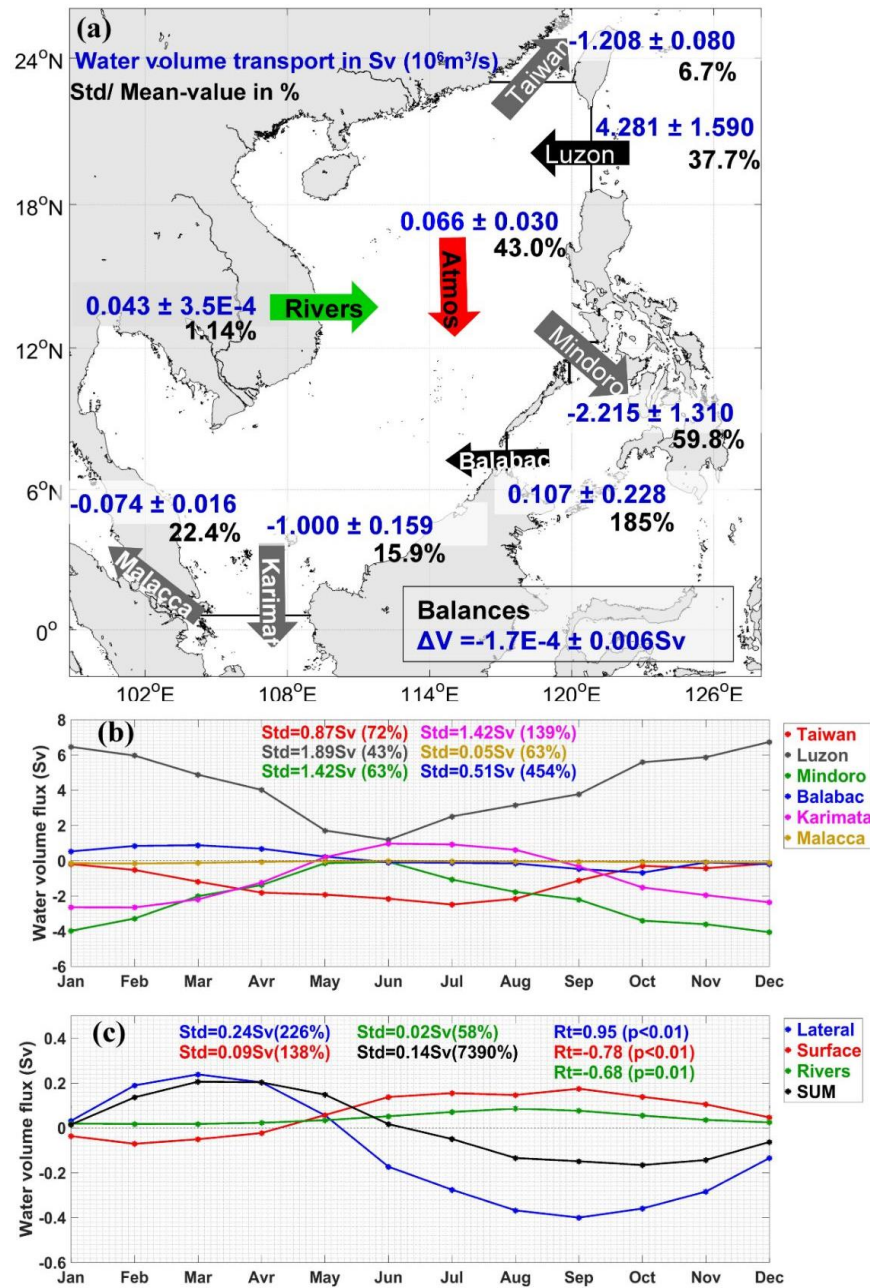
**Table 4: Synthesis of lateral water volume transports (in Sv) through SCS straits obtained from previous numerical and observation studies and from our study. Positive = inflow and negative = outflow.**

	Method / resolution / analyzed period	Luzon	Taiwan	Mindoro	Balabac	Karimata	Malacca
Our study	Model: SYMPHONIE 4km ~ 1/28° 2010-2018	4.28±1.59	-1.21±0.08	-2.22±1.31	0.11±0.23	-1.00±0.16	-0.07±0.02
Metzger and Hurlburt (1996)	Model: NLOM (Reduced gravity 1.5 layer) 1/2° latitude 45/64° longitude 1982-1983	4.4±2.5					
Qu et al. (2004)	Model: MOM2.0 1/4° 1982 - 1998	2.4		-0.7		-1.7 = sum of Karimata and Malacca	
Xue et al. (2004)	Model: POM 9-12km 20 yr climatology	2					
Wu and Hsin (2005)	Model: EAMS 1/8° 1999-2003		-1.09				
Fang et al. (2005)	Model: GFDL MOM2.0 1/6° 10yr climatology	4.37	-0.45	-1.77	-0.61	-1.32	-0.22
Tozuka et al. (2007)	Model: MOM3.0 0.4° 10yr climatology	3.6	-1.8	-0.4		-1.4	
Fang et al. (2009)	Model: MOM2.0 1/6° 1982-2003	4.80	-1.71	-1.35	-0.41	-1.16	-0.16
Yaremchuk et al. (2009)	Model: Reduced gravity 4 <sup>1/2</sup> -layer 0.5° Upper 750 m	2.4±0.6	-0.6±0.5	-1.5±0.4		-0.3±0.5	
Tozuka et al. (2009)	Model: MOM3.0 0.4° - 2° 1980-2006	4.4				-1.6	
Wang et al. (2009)	Model: HYCOM 1/6° 30 yrs climatology	4.5	-2.3	-1.7	0.01	-0.5 (Sunda Shelf transport)	

Metzger et al. (2010)	Model: HYCOM 1/12° 2003-2006						-0.6	-0.08
Liu et al. (2010)	Model: MOM4p0d 1/10°-2° 1995-1999		-1.88±0.32					
Liu et al. (2011)	Model: BRAN 0.1° - 2° 1993-2008	4.81	-1.44	-2.27	0.01		-1.42	-0.27
Xu and Malanotte-Rizzoli (2013)	Model: MITgcm/ -FVCOM 2°/5-18-50km 1960s/1990s	5.6		-2.0			-1.4	
Hsin et al. (2012)	Model: EAMS 1/8° 2002-2008	4.0±5.1	-2.6	-0.9	0.1		-0.8	
Zhang et al. (2014)	Model: 2D barotropic 1/10°-1/30° 2005 - 2008		-0.78±1.29					
Tozuka et al. (2015)	Coupled model: UTCM 0.4°-2° OGCM T42 AGCM 160 yrs climatology	2.9	-1.5	-0.1	0.8		-2.3	
He et al. (2015)	Model, BRAN 0.1° 1996-2006						-1.6	
Daryaboy et al. (2016)	Model: ROMS 9-50 km 10 yr climatology  Observations: SODA dataset						-0.18 -0.29	-0.14 -0.13
Wei et al. (2016)	Model: POM/ATOP 0.1°x0.1° 2004-2012	4.9	-1.1	-2.6			-0.7	
Wang et al. (2019)	Model: GL-Ba008 dataset (HYCOM) 7km 2004-2014  Observations: ADCP 11/2008-06/2015	4.67	-1.6	-2.13			-0.5 -0.74 (mean)	
Wyrcki (1961)	Observations: Dynamics method (1909-1957) Upper 175m	0.5						
Qu (2000)	Observations: Dynamics method (WOA1994) Upper 400 m	3.0						
Chu and Li (2000)	Observations: GDEM/MOODS dataset 1930-1997	6.5						

Tian et al. (2006)	Observations: LADCP/CTD (Oct 2005)	6.0±3.0					
Yuan et al. (2008)	Observations: NCEP/ hydrographic dataset (Aug-Sep 1994)	3.5					
Yang et al. (2010)	Observations: LADCP/CTD (Jul 2007)	-5.5					
Fang et al. (1991)	Observations: Current meters 1980s		-2				
Chung et al. (2001)	Observations: ADCP/CTD (May, Aug 1999)		-2.0 (May) -2.2 (Aug)				
Wang et al. (2003)	Observations: ADCP (1999-2001)		-1.8				
Fang et al. (2010)	Observations: ADCP Jan-Feb 2008					-3.6±0.8	
Susanto et al. (2013)	Observations: ADCP Dec 2007-Nov 2008					-0.5±1.9	
Qu and Song (2009)	Observations: SSH & OBP data (2004-2007)			-2.4			
Sprintall et al. (2012)	Observations: Mooring ADCP (2008)			-0.07			

620 Fig. 11 shows the climatological average over 2010-2018 of the lateral fluxes flowing through the SCS interocean straits, the air-sea surface fluxes, the continental river inputs and the internal yearly variations in our simulation.



625 **Figure 11: (a) 2010-2018 averages and standard deviations of water volume yearly fluxes at interocean straits (black arrow = inflow, gray arrow = outflow), from the atmosphere (red arrow) and from rivers (green arrow). Positive and negative values correspond to inflow and outflow, respectively. In black the ratio (in %) of standard deviation and mean value. The yearly water volume variation in the whole SCS over 2010 - 2018 is provided on the bottom right corner. Time series of**

monthly averages of (b) lateral water volume transport through each strait and of (c) total lateral, river and atmospheric water volume fluxes and their sum (equal to the monthly internal variation, Eq. 1) over the SCS domain. Std and Rt stand for standard deviation and correlation with the sum of fluxes, respectively.

### 5.1.1 Climatological mean values and seasonal cycle

630 In our simulation results, seawater enters the SCS through the Luzon and Balabac Straits and flows out of the basin via the Taiwan, Mindoro, Karimata and Malacca Straits, forming the SCSTF identified by Qu et al. (2005) (Fig. 11a). The main inflow into the SCS is from the Pacific Ocean through the Luzon Strait, with an average simulated water volume inflow of 4.3 Sv, in the range of LST previous numerical estimates that vary between 2.4 and 4.8 Sv (Metzger and Hurlburt 1996, Qu et al. 2004, Xue et al. 2004, Tozuka et al. 2007, 2009, 2015, Fang et al. 2005, 2009, Liu et al. 635 2011, Hsin et al. 2012, Xu and Malanotte-Rizzoli 2013, Wei et al. 2016, Wang et al. 2019 - Table 4) and from previous observational studies, that vary between 3.0 and 6.5 Sv (Qu 2000, Chu and Li 2000 - Table 4).

Fig. 11b illustrates the simulated seasonal cycle of water volume transport through SCS interocean straits. The LST (black line) is positive (westward) all over the year, with a maximum intrusion in winter (December, 6.74 Sv) and a minimum intrusion in summer (June, 1.18 Sv), in agreement with previous numerical studies listed in Table 4 (Metzger and Hurlburt 1996, Qu 2000, Qu et al. 2004, Chu and Li 2000, Fang et al. 2005, Yaremchuk et al. 2009, Liu et al. 640 2011, Xu and Malanotte-Rizzoli 2013, Wang et al. 2019). Our model averaged LST in January (6.46 Sv), August (3.14 Sv) and October (5.58 Sv) is also close to observations of respectively Qu (2000, 5.3 Sv in January - climatology value), Yuan et al. (2008, 3.5 Sv in August 1994), and Tian et al. (2006,  $6\pm 3$  Sv in October 2005).

The model simulates a 1.21 Sv water volume outflow through the Taiwan Strait. This is consistent with numerical 645 outflow estimates varying from 0.45 to 2.6 Sv (Wu and Hsin 2005, Fang et al. 2005, 2009, Tozuka et al. 2007, 2015, Yaremchuk et al. 2009, Wang et al. 2009, Liu et al. 2011, Hsin et al. 2012, Zhang et al. 2014, Wei et al. 2016, Wang et al. 2019, Table 4), as well as with observational estimates of 1.8 - 2.0 Sv (Fang et al. 1991, Wang et al. 2003 - Table 4). This transport is negative the whole year (Fig. 11b, red line), with a maximum 2.50 Sv outflow in July, a decrease in autumn - winter until a minimum 0.16 Sv outflow in December. These results are consistent with numerical 650 estimations of Xue et al. (2004), Fang et al. (2005, 2009), Yaremchuk et al. (2009), Liu et al. (2011), Zhang et al. (2014), Wang et al. (2019) and close to measurements of Wang et al. (2003) who found a maximum outflow of 2.7 Sv in summer and a minimum outflow of 0.9 Sv in winter.

At Mindoro Strait, our model simulates an average lateral seawater outflow of 2.22 Sv, in agreement with estimates from previous modeling studies varying from 0.1 to 2.6 Sv (Liu et al. 2011, Wang et al. 2019, Fang et al. 2009, 655 Yaremchuk et al. 2009, Xu and Malanotte-Rizzoli 2013, Tozuka et al. 2007, 2015 - Table 4). The simulated outflow is also quite close to observations (2.4 Sv) analyzed by Qu and Song (2009), and stronger than in-situ estimates (0.07 Sv) of Sprintall et al. (2012). Similarly to previous studies mentioned above, the model simulates an outflow at Mindoro for the whole year (Fig. 11b, green line), maximum in December (4.05 Sv) and minimum in summer (0.06 Sv outflow in June).

660 In the south of the SCS, our model produces a 1.0 Sv seawater outflow through the Karimata Strait, in agreement with  
previous numerical estimates ranging from 0.3 to 2.3 Sv (Fang et al. 2005, 2009, Yaremchuk et al. 2009, Tozuka et  
al. 2007, 2009, 2015, Wang et al. 2009, Metzger et al. 2010, Liu et al. 2011, Xu and Malanotte-Rizzoli 2013, He et al.  
2015, Daryaboy et al. 2016, Wei et al. 2016, Wang et al. 2019, Table 4) and slightly larger than estimates from  
665 measurements (0.50 to 0.74 Sv). The simulated annual cycle of the Karimata water volume transport (Fig. 11b,  
magenta line) shows a southward outflow from September to April, and a northward inflow from May to August, with  
values ranging from -2.64 Sv in January to 0.97 Sv in June, again in agreement with previous studies (Fang et al. 2005,  
2009, Xue et al. 2004, Yaremchuk et al. 2009, Liu et al. 2011, Xu and Malanotte-Rizzoli 2013, He et al. 2015, Wei et  
al. 2016, Wang et al. 2019, Daryaboy et al. 2016, Susanto et al. 2013, Wang et al. 2019).

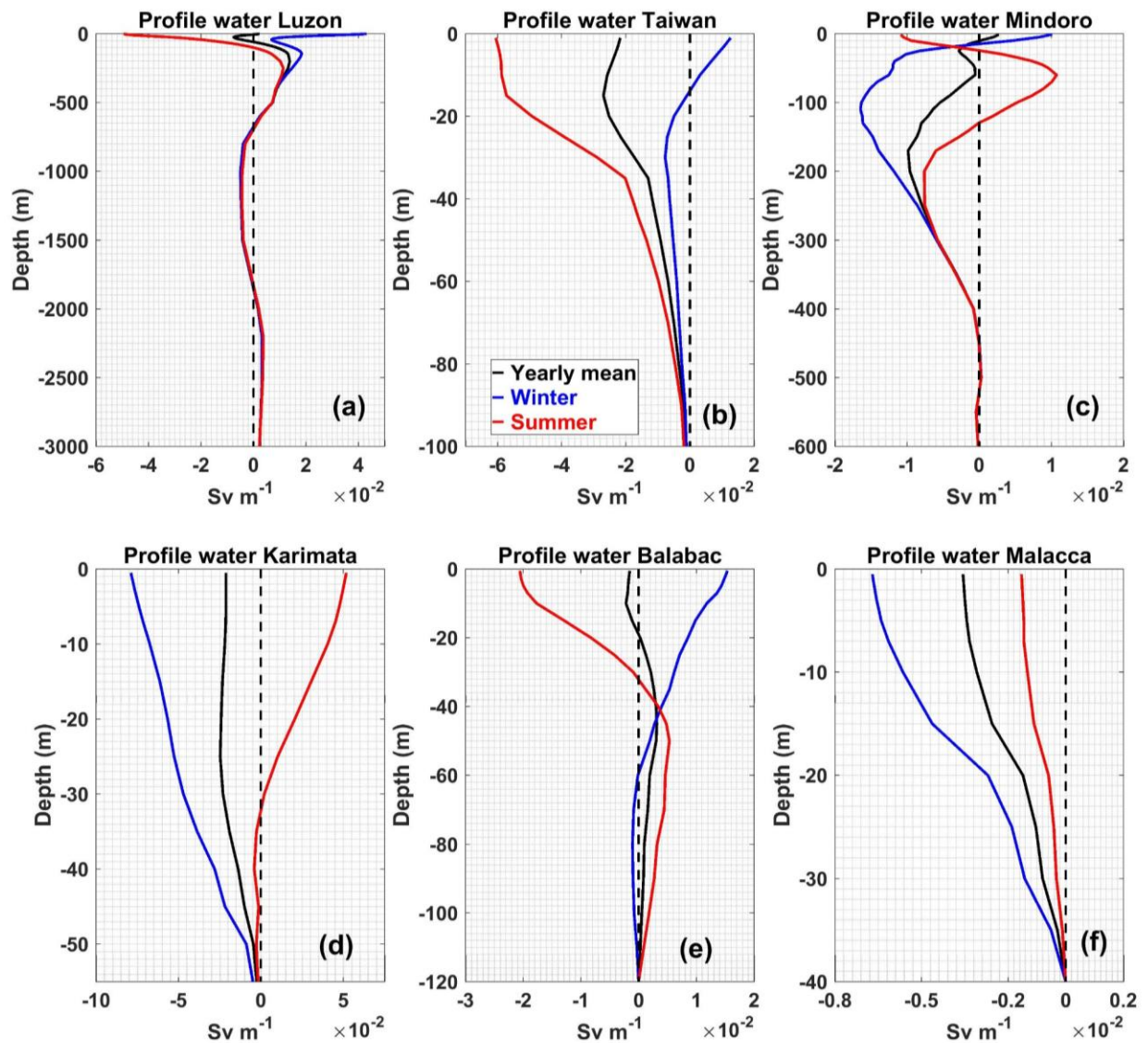
Compared to the four main straits of the SCS, Balabac and Malacca Straits show water volume transports one order  
670 of magnitude smaller (Fig. 11b), and observational studies are scarce. Our simulation produces an annual mean  
westward inflow of 0.11 Sv at Balabac, in agreement with the estimate of 0.1 Sv by Hsin et al. (2012), while Wang et  
al. (2009) and Liu et al. (2011) estimated very small inflows (0.01 Sv) and Tozuka et al. (2015) suggested a much  
stronger inflow (0.8 Sv). Fang et al. (2005, 2009), in contrast, proposed an eastward outflow of, respectively, 0.061  
675 Sv and 0.41 Sv at these channels. In our simulation, water enters at Balabac from January to May (maximum of 0.88  
Sv in March, Fig. 11b, blue line), and exits from June to December (maximum of 0.68 Sv in October). Fang et al.  
(2005, 2009), on the other hand, obtained an outflow the whole year.

At the narrowest interocean strait of the SCS, Malacca, water flows out of the SCS toward the Andaman Sea (Indian  
Ocean) at a rate of 0.07 Sv in our simulation, at the low end of the range of previous estimates (from 0.08 to 0.27 Sv  
- Metzger et al. 2010, Fang et al. 2009, Liu et al. 2011, Daryaboy et al. 2016). The Andaman Sea receives water from  
680 the SCS all over the year in our simulation (maximum 0.16 Sv in February, minimum 0.02 Sv in May and June, Fig.  
11b, cyan line) consistently with model results of Fang et al. (2005, 2009).

Last, the water volume transport at Balabac Strait shows the strongest annual variability over the yearly cycle (Fig.  
11b), with a very high standard deviation relative to the average (0.51 Sv, 454%), followed by Karimata (1.42 Sv,  
139%), Taiwan (0.87 Sv, 72%), Mindoro (1.42 Sv, 63%), Malacca (0.05 Sv, 63%), and Luzon (1.89 Sv, 43%) Straits.

### 685 **5.1.2 Vertical structure**

We examine the vertical distribution of water volume interocean fluxes along the water column for the whole year,  
summer and winter (Fig. 12).



690 **Figure 12:** Yearly (in black) and seasonal (winter: December, January and February, in blue and summer: June, July, August, in red) climatological averages over 2010-2018 of vertical profiles of water volume lateral fluxes via the 6 interoceanic straits ( $\text{Sv}\cdot\text{m}^{-1}$ ). Positive, resp. negative values indicate inflow, resp. outflow. The depth axis varies and is adapted to the depth of the strait.

695 At the largest and deepest strait of the SCS, the Luzon Strait, we simulate a strong seasonal variability of fluxes in the surface and subsurface layers, from 0 to 400 m (Fig. 12a). In the first 50 m, the lateral seawater flux is westward (inflow) in winter and eastward (outflow) in summer, in phase with the seasonal wind forcing (northeast monsoon winds in winter and southwest monsoon winds in summer). This seasonal variability of the surface flow is consistent with observations of Centurioni et al. (2004) obtained from Argo floats data showing an inflow in the upper 15 m from the Pacific to the SCS in winter, but no inflow in summer. The yearly averaged flux is eastward for the upper 50

700 m. In the 50-700 m layer, summer, winter, and yearly mean fluxes are all westward, with a maximum inflow between 100 and 300 m. Until 400 m depth, inflow is stronger in winter, and weaker in summer. Below 400 m depth, we do not obtain any significant seasonal variability. Our simulation produces an outflow for all seasons between 700 and 1900 m (slightly stronger in winter), then a weak inflow in the deep layer (slightly stronger in summer), from 1900 m until the bottom. Qu et al. (2004), Hsin et al. (2012), Nan et al. (2013, 2015), Liu and Gan (2017) found the same vertical structure of water volume transport crossing the Luzon Strait using numerical methods, as well as Li and Qu (2006) using dissolved oxygen distribution data.

The yearly mean water volume fluxes through the Taiwan Strait are negative, i.e. northward, along the whole water column (Fig. 12b). We simulate a strong seasonal variability of vertical distribution of fluxes at this shallow strait, again triggered by the atmospheric forcing. In winter, under the northeast monsoon wind, fluxes flow southward in the surface layer (0-10 m), then underneath this depth, fluxes become northwards. In summer, under the southwest monsoon wind, fluxes are northwards from the surface to the bottom, and particularly strong between 0 and 15 m.

Regarding the Mindoro Strait (Fig. 12c), we simulate a strong seasonal variability of fluxes for the upper 300 m. Deeper than 300 m, we observe no significant seasonal variability of fluxes, which are negligible below 400 m. In winter, fluxes flow inward in the layer 0-20 m, and outward between 20 and 400 m, with a maximum outflow around 120 m. In summer, we obtain a “sandwich” vertical distribution like at the Luzon Strait, with outflows in the upper layer (0-30 m, maximum at the surface) and in the subsurface layer (130-400 m, maximum near 200-250 m) and an inflow between these two layers (30-130 m, maximum near 60 m). Again, winter westward inflow and summer eastward outflow in the surface layer follow the monsoon wind direction. Below 130 m, both winter and summer fluxes flow outward, but the winter outflow is much stronger than the summer one. The annual mean flux shows a small inflow in the first 10 m and an outflow below 10 m, with local maxima at 30 and 180 m depths.

At the shallow Karimata Strait (Fig. 12d), the yearly climatological fluxes are southwards (outflow) over the full depth. Like for the Taiwan Strait, fluxes through the Karimata Strait strongly vary with the seasonal monsoon summer southwest and winter northeast winds. In summer, fluxes enter the basin above 30 m depth, then slightly flow out in the deepest layer until 55 m depth. In winter, fluxes are southwards all along the water column. This simulated seasonal variability of vertical fluxes is in agreement with *in-situ* measurements of Fang et al. (2010), who found that the monsoon was the main factor influencing the fluxes at the Karimata Strait.

The vertical structure of fluxes across the shallow Balabac Strait also connecting the SCS with the Sulu Sea also varies strongly with the seasonal cycle (Fig. 12e). In winter, the (westward) inflow is maximum at the surface then decreases with depth. From 60 m depth to the bottom, the winter flux becomes slightly negative. The situation is opposite in summer: fluxes flow eastward (outflow) in the surface layer with a decrease with depth until 30 m, then flow westward from 30 m depth until the bottom. The annual mean fluxes are negative for the upper 20 m, then positive until the bottom (with a maximum inflow at 40 m depth).



Fluxes crossing the Malacca Strait flow westward (outflow) all year round along the whole water column, with stronger values near the surface, and a decrease with depth, and stronger fluxes in winter (Fig. 12f). As the section is very shallow (40 m depth), the monsoon wind again plays an important role in the difference of seasonal fluxes intensity: the northeast wind reinforces the outflow in winter, and the southwest monsoon reduces it in summer.

## 5.2 Contributions of surface, river and lateral interocean fluxes to the SCS water volume budget

In this section we analyze the water volume budget obtained from our simulation and quantify the contributions of each term of Eq. 1 to the internal variations of water volume in the SCS: lateral fluxes flowing through the SCS interocean straits, air-sea surface fluxes and continental inputs from rivers.

The average net seawater volume exchanged through SCS interocean straits over the period 2010 - 2018 in our simulation is equal to  $-0.11$  Sv (Fig. 11a). This net lateral loss at the domain oceanic open boundaries is balanced by the inputs from rivers and atmosphere, evaluated respectively at  $0.04$  Sv and  $0.07$  Sv, i.e. a total freshwater volume input of  $0.11$  Sv (Fig. 11a). The difference between the gain from atmosphere and rivers and the loss from straits, i.e. the water volume variation, is equal to  $-1.7e-4$  Sv, equivalent to a decrease of sea level of  $1.6$  mm year<sup>-1</sup> over the period 2010-2018 and negligible compared to the total water volume input (0.004%). Our value of atmospheric freshwater flux is slightly smaller than estimates of Qu et al. (2006) who provided an annual mean value of  $0.1 - 0.2$  Sv through analyzes of several dataset of precipitation (CMAP, GPCP, TRMM) and evaporation (NCEP reanalysis). Fang et al. (2009) deduced from the land discharges relation of Perry et al. (1996) an annual river flux of  $0.05$  Sv, close to our yearly river water volume flux. Using numerical models, Qu et al. (2006), Fang et al. (2009) and Wang et al. (2019) obtained a yearly average of total freshwater flux over the whole SCS respectively of  $0.08$  Sv (period 1950 - 2003),  $0.11$  Sv (period 1982 - 2003) and  $0.11$  Sv (period 2008 - 2015), quite close to our model result. These previous studies assumed a null total lateral water volume flux and calculated the total freshwater flux based on the lateral salt budget and the mean salinity of the whole basin.

Fig. 11c illustrates the 10-year climatological monthly averages of all the water volume fluxes exchanged between the SCS and surrounding environment in our simulation: the total interocean lateral flux, river runoff, surface atmospheric flux, and the sum of all three fluxes, which equals the internal water volume variation (Eq. 1). The total lateral flux is positive (inflows > outflows) from January to May and negative (inflows < outflows) the rest of the year. The strongest net lateral inflow occurs in March ( $0.24$  Sv) and the strongest outflow in September ( $-0.40$  Sv). Atmospheric and river fluxes are out of phase with those lateral fluxes. Surface fluxes are negative during the winter - spring dry season (with a maximum surface loss in February,  $-0.07$  Sv) when evaporation dominates precipitation. During the summer - autumn rainy season, precipitation becomes abundant, the surface fluxes become positive (maximum value in September  $0.17$  Sv) and the freshwater river flux increases from May to October with a maximum in August ( $0.09$  Sv).

765 To better understand the role of the SCS in the global and regional water cycle, we analyze the sum of the water  
volume fluxes (Fig. 11c, black curve) exchanged yearly over the domain, equal to the water volume variation. In  
overall, the SCS stores water from January to June (with a maximum 0.21 Sv storage in March and April) and releases  
water from July to December (minimum of -0.17 Sv in October). The correlations between monthly oceanic lateral,  
770 surface and river fluxes and the total water monthly flux are respectively 0.95 ( $p < 0.01$ ), -0.78 ( $p < 0.01$ ) and -0.68  
( $p = 0.02$ ). The lateral winter gain (and summer lateral loss) largely exceeds the atmospheric winter loss (and summer  
atmospheric and river gain). Moreover, the standard deviation of the climatological monthly total lateral flux (0.24  
Sv) is about three times higher than the standard deviation of atmospheric fluxes (0.09 Sv) and 10 times higher than  
the standard deviation of river fluxes (0.02 Sv). Over an annual cycle, the monthly variability of the lateral flux, which  
is strongly driven by monsoon winds, therefore dominates the variability of the two other fluxes (atmospheric and  
775 river) and drives the annual cycle of the SCS water storage. The low variability of river fluxes compared to lateral and  
surface fluxes is partly explained by the use of monthly climatology river runoff for most of the rivers in our  
simulation, especially for huge rivers such as the Mekong and Pearl rivers.

## 6. Conclusion

The three-dimensional hydrodynamic model SYMPHONIE was implemented over the South China Sea with high  
780 horizontal resolution (4 km) and an explicit representation of tides to simulate and study the functioning, variability  
and influence of ocean circulation in the SCS and their role in regional climate.

A simulation was performed over the recent 9-year period 2010 – 2018, using three hourly atmospheric forcing, daily  
lateral oceanic boundary forcing, nine tidal forcing components and real-time or climatology data for 63 river  
discharge points. The ability of the model to reproduce the characteristics of circulation and water masses over the  
785 SCS, including tides, was evaluated through a thorough comparison with available satellite and in-situ observation  
datasets and with simulations performed with other models at coarser resolution. The model shows good performances  
in terms of tidal cycle and of seasonal cycle, interannual variability and spatial distribution of surface characteristics  
and circulation (SST, SSS, SLA and associated geostrophic currents). Comparisons with Argo and glider profiles and  
other models showed that SYMPHONIE reproduces well the vertical distributions of temperature and salinity as well  
790 as MLD. These comparisons with observational data and other models therefore quantitatively show the added-value  
of this high-resolution hydrodynamic model that includes tides for the representation and study of the spatial and  
temporal variability of the SCS dynamics and water masses.

One of the first objectives of this numerical tool is to study the variability of the water volume, heat and salt budgets  
at different scales, precisely quantifying the contribution of each component: lateral oceanic, surface atmospheric and  
795 river fluxes, internal variations. We implemented an online computation method allowing to rigorously close those  
budgets: over any given period, and for all the quantities studied, the sum of all fluxes is equal to the variation of the  
quantity over the period. We quantitatively demonstrated the added-value of the online method. With offline

computation based on daily outputs, NRMSE reaches 10 to 30% for interannual variations of yearly values of heat and salt net lateral fluxes. Moreover, the online method allows to rigorously compute at each lateral strait the total inflowing and outflowing fluxes, contrary to the offline method that induces errors of the same order or even one order of magnitude larger than the values themselves.

This simulation was then used to provide a new quantitative insight on the SCSTF and SCS water volume budgets at the seasonal and climatological scales. Estimates over the 2010-2018 period of the water volume transports through SCS interocean straits and of their seasonal cycle and vertical distributions, and of each term of the volume budget over the whole domain were examined and compared with a synthesis of previous estimates. They were shown to be in agreement with available observational and numerical studies. According to our simulation, the SCS receives over the period 2010 – 2018 an annual average 4.50 Sv water input, mainly from the Western Pacific through the Luzon Strait (4.28 Sv, 95%). The remaining input comes from the Sulu Sea through the Balabac Strait (3%), from the atmosphere (1%) and from rivers (1%). The SCS releases all of this water through the other straits: half of the water flows to the Sulu Sea through the Mindoro Strait, about one quarter flows northward to the East China Sea via the Taiwan Strait (27%), and one quarter flows southwestward to the Java Sea through the Karimata Strait (22%). Taking the sum of fluxes through the Mindoro, Balabac, Karimata and Malacca Straits (following Fang et al. 2009, He et al. 2015, Wei et al. 2016), we provide a 3.2 Sv estimate for the water volume transport from the SCS into the Indian Ocean: 70% of the total water input to the SCS is transferred toward the Indian Ocean. The analysis of the seasonal cycle of SCSTF and SCS water budgets shows that from February to July, the SCS stores water. This water gain first comes from lateral fluxes (February to April), mainly through the Luzon Strait, then to a lesser extent from rivers and atmospheric freshwater fluxes (May to July). From August to January, the SCS loses water: it receives water from the atmosphere and rivers but releases a larger amount of water through lateral fluxes, mostly through the Taiwan, Mindoro and Karimata Straits, with a peak outflow in August-September. The SCS is a source of water to the atmosphere from January to April (evaporation exceeds precipitation), and a sink from May to December. Interocean exchanges, as well as their vertical structures, show seasonal variations that weaken when depth increases and are driven by monsoon winds. Exchanges at Luzon, Mindoro and Karimata Straits are enhanced during the autumn-winter period, from October to February, and weakened during the spring summer period, from April to September (and even reversed for Karimata), due to the opposite effects of the winter northeast monsoon winds (that favor eastward and southward flows) and of the southwest monsoon winds (that favor westward and southward flows). The situation is the opposite at Taiwan Strait, where the winter northeast monsoon weakens the northward outflow whereas the summer southwest monsoon enhances it. Exchanges through Luzon Strait deep layers show a stable sandwiched structure with vertically alternating inflows and outflows. Finally, seasonal variations of SCS water content are completely driven by the lateral oceanic water volume fluxes through interocean straits, themselves driven by seasonal monsoons.

This 9-year SCS simulation from a high-resolution model producing a consistent closed water volume, heat and salt budgets will now be used to examine in detail the interannual variability of those budgets over the region. Except at

Taiwan Strait, interocean and atmospheric water volume fluxes indeed vary strongly on an interannual time scale: standard deviations of yearly fluxes can be of the same order of magnitude as mean values, reaching 38% and 60% at Luzon and Mindoro Straits, and even 185% at Balabac Strait (Fig. 11a). These important variations partly explain the uncertainties of numerical and observational estimates. In addition, a decrease of SSS over the period 2011-2012 followed by an increase until 2016 were observed over the SCS by Zeng et al. (2014, 2018), and attributed to an increase of precipitations and a reduced intrusion of the Kuroshio salty water mass at Luzon Strait, followed by a decrease of precipitations and a stronger Luzon inflow. Those SSS interannual variations are well reproduced by our simulation, that will be used to examine and explain them in detail.

The simulation presented here is fully available to the interested scientific community. Using this hydrodynamical numerical tool to model and understand the SCS ocean dynamics will allow us to examine their influence on other compartments of the regional system. A coupling with a biogeochemical model (Herrmann et al. 2014, 2017) would allow to study the functioning and variability of SCS planktonic ecosystem, which are strongly influenced by ocean dynamics (Bombar et al. 2010; Loisel et al. 2017; Lu et al. 2018). This simulation, or simulation performed over given periods of interests, could also be used to assess the dispersion of potential contaminants over the area (plastics, radioactive contaminants, etc. e.g., Estournel et al. 2012). A coupling with a regional atmospheric model, that will allow to consider and examine the contributions of air-sea interactions in the ocean and atmosphere dynamics in the region, is also under development over the Southeast Asia region to be integrated in the framework of the CORDEX-SEA project (Tangang et al. 2020; Herrmann et al. 2022).

### **Code and data availability**

The SYMPHONIE hydrodynamical ocean model version 2.4, the SCS configuration, input files, data for model assessment and code used to generate figures are freely available on <https://doi.org/10.5281/zenodo.7941495> (Trinh et al. 2023).

### **855 Author contribution**

Trinh Bich Ngoc, Marine Herrmann and Caroline Ulises designed the experiments and Trinh Bich Ngoc carried them out, with the support of Thomas Duhaut, Patrick Marsaleix and Claude Estournel. Patrick Marsaleix, Thomas Duhaut and Claude Estournel developed the model code. Trinh Bich Ngoc, To Duy Thai, and Patrick Marsaleix worked on the model calibration and optimization. Trinh Bich Ngoc, Claude Estournel and Patrick Marsaleix implemented and analyzed the online and offline computational methods. R. Kipp Shearman organized the seaglider survey. Trinh Bich Ngoc, Marine Herrmann and Caroline Ulises prepared the manuscript with contributions from all coauthors.

## Competing interest

The authors declare that they have no conflict of interest.

## Acknowledgments

865 This work is a part of LOTUS international joint laboratory (lotus.usth.edu.vn) funded by IRD. Numerical simulations were performed using CALMIP HPC facilities (projects P13120 and p20055) and the cluster OCCIGEN from the CINES group (project DARI A0080110098). This work is also supported by the Vietnam Academy of Science and Technology, grant code CSCL17.03/23-24. The authors would like to thank the SIROCCO service (<https://sirocco.obs-mip.fr/>), coordinated by the Research Infrastructure ILICO (CNRS-IFREMER), for providing the  
870 SYMPHONIE code.

## References

- Ablain, M., Cazenave, A., Larnicol, G., Balmaseda, M., Cipollini, P., Faugère, Y., Fernandes, M. J., Henry, O., Johannessen, J. A., Knudsen, P., Andersen, O., Legeais, J., Meyssignac, B., Picot, N., Roca, M., Rudenko, S., Scharffenberg, M. G., Stammer, D., Timms, G., and Benveniste, J.: Improved sea level record over the satellite altimetry era (1993–2010) from the Climate Change Initiative project, *Ocean Science*, 11, 67–82, <https://doi.org/10.5194/os-11-67-2015>, 2015.
- Bombar, D., Dippner, J. W., Doan, H. N., Ngoc, L. N., Liskow, I., Loick-Wilde, N., and Voss, M.: Sources of new nitrogen in the Vietnamese upwelling region of the South China Sea, *J Geophys Res Oceans*, 115, <https://doi.org/10.1029/2008JC005154>, 2010.
- 880 Boutin, J., Martin, N., Kolodziejczyk, N., and Reverdin, G.: Interannual anomalies of SMOS sea surface salinity, *Remote Sens Environ*, 180, 128–136, <https://doi.org/10.1016/j.rse.2016.02.053>, 2016.
- Carrère, L., Lyard, F., Cancet, M., Guillot, A., Picot, N.: FES2014, a new tidal model - Validation results and perspectives for improvements, presentation to ESA Living Planet Conference, Prague, 2016.
- Centurioni, L. R., Niiler, P. P., and Lee, D. K.: Observations of inflow of Philippine sea surface water into the South  
885 China Sea through the Luzon strait, *J Phys Oceanogr*, 34, [https://doi.org/10.1175/1520-0485\(2004\)034<0113:OOIOPS>2.0.CO;2](https://doi.org/10.1175/1520-0485(2004)034<0113:OOIOPS>2.0.CO;2), 2004.
- Chassignet, E. P., Xu, X., Bozec, A., and Uchida, T.: Impact of the New England Seamount Chain on Gulf Stream Pathway and Variability, *J Phys Oceanogr*, 53, <https://doi.org/10.1175/JPO-D-23-0008.1>, 2023.
- Chen, C. T. A., Hou, W. P., Gamo, T., and Wang, S. L.: Carbonate-related parameters of subsurface waters in the  
890 West Philippine, South China and Sulu Seas, *Mar Chem*, 99, 151–161, <https://doi.org/10.1016/j.marchem.2005.05.008>, 2006.

- Chen, G., Hou, Y., and Chu, X.: Mesoscale eddies in the South China Sea: Mean properties, spatiotemporal variability, and impact on thermohaline structure, *J Geophys Res Oceans*, 116, 1–19, <https://doi.org/10.1029/2010JC006716>, 2011.
- 895 Chu, P. C. and Li, R.: South China Sea isopycnal-surface circulation, *J Phys Oceanogr*, 30, 2419–2438, [https://doi.org/10.1175/1520-0485\(2000\)030<2419:SCSISC>2.0.CO;2](https://doi.org/10.1175/1520-0485(2000)030<2419:SCSISC>2.0.CO;2), 2000.
- Chung, S. W., Jan, S., and Liu, K. K.: Nutrient fluxes through the Taiwan Strait in spring and summer 1999, *J Oceanogr*, 57, <https://doi.org/10.1023/A:1011122703552>, 2001.
- CIESIN: Gridded Population of the World, Version 4 (GPWv4): Basic Characteristics, Revision 11. Palisades, NY: NASA Socioeconomic Data and Applications Center (SEDAC), Columbia University Center for International Earth  
900 Science Information Network (CIESIN) - Columbia University, 2018.
- Costa, A., Doglioli, A. M., Marsaleix, P., and Petrenko, A. A.: Comparison of in situ microstructure measurements to different turbulence closure schemes in a 3-D numerical ocean circulation model, *Ocean Model (Oxf)*, 120, <https://doi.org/10.1016/j.ocemod.2017.10.002>, 2017.
- 905 Da, N. D., Herrmann, M., Morrow, R., Niño, F., Huan, N. M., and Trinh, N. Q.: Contributions of Wind, Ocean Intrinsic Variability, and ENSO to the Interannual Variability of the South Vietnam Upwelling: A Modeling Study, *J Geophys Res Oceans*, 124, 6545–6574, <https://doi.org/10.1029/2018JC014647>, 2019.
- Daryabor, F., Ooi, S. H., Samah, A. A., and Akbari, A.: Dynamics of the water circulations in the Southern South China Sea and its seasonal transports, *PLoS One*, 11, 1–20, <https://doi.org/10.1371/journal.pone.0158415>, 2016.
- 910 Estournel, C., Bosc, E., Bocquet, M., Ulses, C., Marsaleix, P., Winiarek, V., Osvath, I., Nguyen, C., Duhaut, T., Lyard, F., Michaud, H., and Auclair, F.: Assessment of the amount of cesium-137 released into the Pacific Ocean after the Fukushima accident and analysis of its dispersion in Japanese coastal waters, *J Geophys Res Oceans*, 117, <https://doi.org/10.1029/2012JC007933>, 2012.
- Estournel, C., Marsaleix, P., and Ulses, C.: A new assessment of the circulation of Atlantic and Intermediate Waters  
915 in the Eastern Mediterranean, *Prog Oceanogr*, 198, <https://doi.org/10.1016/j.pocean.2021.102673>, 2021.
- Fang, G., Zhao, B., and Zhu, Y.: Water volume transport through the taiwan strait and the continental skelf of the east china sea measured with current meters, *Elsevier Oceanography Series*, 54, 345–358, [https://doi.org/10.1016/S0422-9894\(08\)70107-7](https://doi.org/10.1016/S0422-9894(08)70107-7), 1991.
- Fang, G., Susanto, D., Soesilo, I., Zheng, Q., Qiao, F., and Wei, Z.: A note on the South China Sea shallow interocean  
920 circulation, *Adv Atmos Sci*, 22, 946–954, <https://doi.org/10.1007/bf02918693>, 2005.
- Fang, G., Wang, Y., Wei, Z., Fang, Y., Qiao, F., and Hu, X.: Interocean circulation and heat and freshwater budgets of the South China Sea based on a numerical model, *Dynamics of Atmospheres and Oceans*, 47, 55–72, <https://doi.org/10.1016/j.dynatmoce.2008.09.003>, 2009.
- Fang, G., Susanto, R. D., Wirasantosa, S., Qiao, F., Supangat, A., Fan, B., Wei, Z., Sulistiyo, B., and Li, S.: Volume,  
925 heat, and freshwater transports from the South China Sea to Indonesian seas in the boreal winter of 2007–2008, *J Geophys Res Oceans*, 115, 1–11, <https://doi.org/10.1029/2010JC006225>, 2010.

- Gan, J., Li, H., Curchitser, E. N., and Haidvogel, D. B.: Modeling South China Sea circulation: Response to seasonal forcing regimes, *J Geophys Res Oceans*, 111, 1–20, <https://doi.org/10.1029/2005JC003298>, 2006.
- Gan, J., Liu, Z., and Hui, C. R.: A three-layer alternating spinning circulation in the South China Sea, *J Phys Oceanogr*, 46, 2309–2315, <https://doi.org/10.1175/JPO-D-16-0044.1>, 2016.
- 930 Garau, B., Ruiz, S., Zhang, W. G., Pascual, A., Heslop, E., Kerfoot, J., and Tintoré, J.: Thermal lag correction on slocum CTD glider data, *J Atmos Ocean Technol*, 28, <https://doi.org/10.1175/JTECH-D-10-05030.1>, 2011.
- Gordon, A. L., Tessler, Z. D., and Villanoy, C.: Dual overflows into the deep Sulu Sea, *Geophys Res Lett*, 38, 1–6, <https://doi.org/10.1029/2011GL048878>, 2011.
- 935 Griffies, S. M. and Hallberg, R. W.: Biharmonic friction with a Smagorinsky-like viscosity for use in large-scale eddy-permitting ocean models, *Mon Weather Rev*, 128, [https://doi.org/10.1175/1520-0493\(2000\)128<2935:bfwasl>2.0.co;2](https://doi.org/10.1175/1520-0493(2000)128<2935:bfwasl>2.0.co;2), 2000.
- Guohong, F.: Tide and tidal current charts for the marginal seas adjacent to China, *Chinese Journal of Oceanology and Limnology*, 4, <https://doi.org/10.1007/BF02850393>, 1986.
- 940 Haigh, I. D., Marcos, M., Talke, S. A., Woodworth, P. L., Hunter, J. R., Hague, B. S., Arns, A., Bradshaw, E., and Thompson, P.: GESLA Version 3: A major update to the global higher-frequency sea-level dataset, *Geosci Data J*, 10, <https://doi.org/10.1002/gdj3.174>, 2023.
- Hatayama, T., Awaji, T., and Akitomo, K.: Tidal currents in the Indonesian Seas and their effect on transport and mixing, *J Geophys Res Oceans*, 101, <https://doi.org/10.1029/96JC00036>, 1996.
- 945 He, Z., Feng, M., Wang, D., and Slawinski, D.: Contribution of the Karimata Strait transport to the Indonesian Throughflow as seen from a data assimilation model, *Cont Shelf Res*, 92, 16–22, <https://doi.org/10.1016/j.csr.2014.10.007>, 2015.
- Herrmann, M., Estournel, C., Adloff, F., and Diaz, F.: Impact of climate change on the northwestern Mediterranean Sea pelagic planktonic ecosystem and associated carbon cycle, *J Geophys Res Oceans*, 119, <https://doi.org/10.1002/2014JC010016>, 2014.
- 950 Herrmann, M., Auger, P. A., Ulses, C., and Estournel, C.: Long-term monitoring of ocean deep convection using multisensors altimetry and ocean color satellite data, *J Geophys Res Oceans*, 122, <https://doi.org/10.1002/2016JC011833>, 2017.
- Herrmann, M., Ngo-Duc, T., and Trinh-Tuan, L.: Impact of climate change on sea surface wind in Southeast Asia, from climatological average to extreme events: results from a dynamical downscaling, *Clim Dyn*, 54, <https://doi.org/10.1007/s00382-019-05103-6>, 2020.
- 955 Herrmann, M., Nguyen-Duy, T., Ngo-Duc, T., and Tangang, F.: Climate change impact on sea surface winds in Southeast Asia, *International Journal of Climatology*, 42, <https://doi.org/10.1002/joc.7433>, 2022.
- Herrmann, M., To Duy, T., and Estournel, C.: Intraseasonal variability of the South Vietnam upwelling, South China Sea: Influence of atmospheric forcing and ocean intrinsic variability, *Ocean Science*, 19, <https://doi.org/10.5194/os-19-453-2023>, 2023.
- 960

- Ho, C. R., Zheng, Q., Soong, Y. S., Kuo, N. J., and Hu, J. H.: Seasonal variability of sea surface height in the South China Sea observed with TOPEX/Poseidon altimeter data, *J Geophys Res Oceans*, 105, 13981–13990, <https://doi.org/10.1029/2000jc900001>, 2000.
- 965 Hsin, Y. C., Wu, C. R., and Chao, S. Y.: An updated examination of the Luzon Strait transport, *J Geophys Res Oceans*, 117, <https://doi.org/10.1029/2011JC007714>, 2012.
- Jackett, D. R., McDougall, T. J., Feistel, R., Wright, D. G., and Griffies, S. M.: Algorithms for density, potential temperature, conservative temperature, and the freezing temperature of seawater, *J Atmos Ocean Technol*, 23, 1709–1728, <https://doi.org/10.1175/JTECH1946.1>, 2006.
- 970 Kumar, A., Jha, B., and L’Heureux, M.: Are tropical SST trends changing the global teleconnection during La Niña?, *Geophys Res Lett*, 37, <https://doi.org/10.1029/2010GL043394>, 2010.
- Large, W. G., and S. Yeager.: Diurnal to decadal global forcing for ocean and sea-ice models: the data sets and flux climatologies. NCAR Technical Note, NCAR/TN-460+STR, CGD Division of the National Center for Atmospheric Research, 2004.
- 975 Laurent, L. S.: Turbulent dissipation on the margins of the South China Sea, *Geophys Res Lett*, 35, <https://doi.org/10.1029/2008GL035520>, 2008.
- Leonard, B. P.: A stable and accurate convective modelling procedure based on quadratic upstream interpolation, *Comput Methods Appl Mech Eng*, 19, [https://doi.org/10.1016/0045-7825\(79\)90034-3](https://doi.org/10.1016/0045-7825(79)90034-3), 1979.
- Li, L. and Qu, T.: Thermohaline circulation in the deep South China Sea basin inferred from oxygen distributions, *J Geophys Res Oceans*, 111, 1–10, <https://doi.org/10.1029/2005JC003164>, 2006.
- 980 Lin, H., Liu, Z., Hu, J., Menemenlis, D., and Huang, Y.: Characterizing meso- to submesoscale features in the South China Sea, *Prog Oceanogr*, 188, <https://doi.org/10.1016/j.pocean.2020.102420>, 2020.
- Liu, K. K., Chao, S. Y., Shaw, P. T., Gong, G. C., Chen, C. C., and Tang, T. Y.: Monsoon-forced chlorophyll distribution and primary production in the South China Sea: Observations and a numerical study, *Deep Sea Res 1*
- 985 *Oceanogr Res Pap*, 49, 1387–1412, [https://doi.org/10.1016/S0967-0637\(02\)00035-3](https://doi.org/10.1016/S0967-0637(02)00035-3), 2002.
- Liu, K. K., Kang, C. K., Kobari, T., Liu, H., Rabouille, C., and Fennel, K.: Biogeochemistry and ecosystems of continental margins in the western North Pacific Ocean and their interactions and responses to external forcing - An overview and synthesis, *Biogeosciences*, 11, 7061–7075, <https://doi.org/10.5194/bg-11-7061-2014>, 2014.
- Liu, N., Eden, C., Dietze, H., Wu, D., and Lin, X.: Model-based estimate of the heat budget in the East China Sea, *J Geophys Res Oceans*, 115, 1–11, <https://doi.org/10.1029/2009JC005869>, 2010.
- 990 Liu, Q., Kaneko, A., and Jilan, S.: Recent progress in studies of the South China Sea circulation, <https://doi.org/10.1007/s10872-008-0063-8>, 2008.
- Liu, Q., Feng, M., and Wang, D.: ENSO-induced interannual variability in the southeastern South China Sea, *J Oceanogr*, 67, 127–133, <https://doi.org/10.1007/s10872-011-0002-y>, 2011.
- 995 Liu, Y., Tang, D., and Evgeny, M.: Chlorophyll concentration response to the typhoon wind-pump induced upper ocean processes considering air-sea heat exchange, *Remote Sens (Basel)*, 11, <https://doi.org/10.3390/rs11151825>, 2019.



- Liu, Z. and Gan, J.: Three-dimensional pathways of water masses in the South China Sea: A modeling study, *J Geophys Res Oceans*, 122, <https://doi.org/10.1002/2016JC012511>, 2017.
- 1000 Loisel, H., Vantrepotte, V., Ouillon, S., Ngoc, D. D., Herrmann, M., Tran, V., Mériaux, X., Dessailly, D., Jamet, C., Duhaut, T., Nguyen, H. H., and van Nguyen, T.: Assessment and analysis of the chlorophyll-a concentration variability over the Vietnamese coastal waters from the MERIS ocean color sensor (2002–2012), *Remote Sens Environ*, 190, 217–232, <https://doi.org/10.1016/j.rse.2016.12.016>, 2017.
- Lu, W., Oey, L. Y., Liao, E., Zhuang, W., Yan, X. H., and Jiang, Y.: Physical modulation to the biological productivity in the summer Vietnam upwelling system, *Ocean Science*, 14, <https://doi.org/10.5194/os-14-1303-2018>, 2018.
- 1005 Lyard, F., Lefevre, F., Letellier, T., and Francis, O.: Modelling the global ocean tides: Modern insights from FES2004, *Ocean Dyn*, 56, <https://doi.org/10.1007/s10236-006-0086-x>, 2006.
- Lyard, F. H., Allain, D. J., Cancet, M., Carrère, L., and Picot, N.: FES2014 global ocean tide atlas: Design and performance, *Ocean Science*, 17, <https://doi.org/10.5194/os-17-615-2021>, 2021.
- 1010 Marsaleix, P., Auclair, F., and Estournel, C.: Considerations on open boundary conditions for regional and coastal ocean models, *J Atmos Ocean Technol*, 23, 1604–1613, <https://doi.org/10.1175/JTECH1930.1>, 2006.
- Marsaleix, P., Auclair, F., Floor, J. W., Herrmann, M. J., Estournel, C., Pairaud, I., and Ulses, C.: Energy conservation issues in sigma-coordinate free-surface ocean models, *Ocean Model (Oxf)*, 20, 61–89, <https://doi.org/10.1016/j.ocemod.2007.07.005>, 2008.
- 1015 Marsaleix, P., Auclair, F., and Estournel, C.: Low-order pressure gradient schemes in sigma coordinate models: The seamount test revisited, *Ocean Model (Oxf)*, 30, 169–177, <https://doi.org/10.1016/j.ocemod.2009.06.011>, 2009.
- Marsaleix, P., Michaud, H., and Estournel, C.: 3D phase-resolved wave modelling with a non-hydrostatic ocean circulation model, *Ocean Model (Oxf)*, 136, 28–50, <https://doi.org/10.1016/j.ocemod.2019.02.002>, 2019.
- Metzger, E. J. and Hurlburt, H. E.: Coupled dynamics of the South China Sea, the Sulu Sea, and the Pacific Ocean, *J Geophys Res Oceans*, 101, 12331–12352, <https://doi.org/10.1029/95JC03861>, 1996.
- 1020 Metzger, E. J., Hurlburt, H. E., Xu, X., Shriver, J. F., Gordon, A. L., Sprintall, J., Susanto, R. D., and van Aken, H. M.: Simulated and observed circulation in the Indonesian Seas: 1/12° global HYCOM and the INSTANT observations, *Dynamics of Atmospheres and Oceans*, 50, 275–300, <https://doi.org/10.1016/j.dynatmoce.2010.04.002>, 2010.
- Nan, F., Xue, H., Chai, F., Wang, D., Yu, F., Shi, M., Guo, P., and Xiu, P.: Weakening of the kuroshio intrusion into the south china sea over the past two decades, *J Clim*, 26, 8097–8110, <https://doi.org/10.1175/JCLI-D-12-00315.1>, 2013.
- 1025 Nan, F., Xue, H., and Yu, F.: Kuroshio intrusion into the South China Sea: A review, *Prog Oceanogr*, 137, 314–333, <https://doi.org/10.1016/j.pocean.2014.05.012>, 2015.
- Nguyen-Duy, T., Ayoub, N. K., Marsaleix, P., Toublanc, F., de Mey-Frémaux, P., Piton, V., Herrmann, M., Duhaut, T., Tran, M. C., and Ngo-Duc, T.: Variability of the Red River Plume in the Gulf of Tonkin as Revealed by Numerical Modeling and Clustering Analysis, *Front Mar Sci*, 8, <https://doi.org/10.3389/fmars.2021.772139>, 2021.
- 1030 Ni, Q., Zhai, X., Wilson, C., Chen, C., and Chen, D.: Submesoscale Eddies in the South China Sea, *Geophys Res Lett*, 48, <https://doi.org/10.1029/2020GL091555>, 2021.

- Pairaud, I. L., Lyard, F., Auclair, F., Letellier, T., and Marsaleix, P.: Dynamics of the semi-diurnal and quarter-diurnal internal tides in the Bay of Biscay. Part 1: Barotropic tides, *Cont Shelf Res*, 28, <https://doi.org/10.1016/j.csr.2008.03.004>, 2008.
- Pairaud, I. L., Auclair, F., Marsaleix, P., Lyard, F., and Pichon, A.: Dynamics of the semi-diurnal and quarter-diurnal internal tides in the Bay of Biscay. Part 2: Baroclinic tides, *Cont Shelf Res*, 30, <https://doi.org/10.1016/j.csr.2009.10.008>, 2010.
- Pan, J. and Sun, Y.: Estimate of ocean mixed layer deepening after a typhoon passage over the south china sea by using satellite data, *J Phys Oceanogr*, 43, 498–506, <https://doi.org/10.1175/JPO-D-12-01.1>, 2013.
- Penjan, R., Siriporn, P., and Natinee, N.: Temperature , Salinity , Dissolved Oxygen and Water Masses of Vietnamese Waters, Proceeding of the SEAFDEC Seminar on Fisheries resources in the South China Sea area IV, Vietnamese Waters. Thailand: South- east Asian Fisheries Development Center, 346–355, 1997.
- Perry, G. D., Duffy, P. B., and Miller, N. L.: An extended data set of river discharges for validation of general circulation models, *Journal of Geophysical Research Atmospheres*, 101, <https://doi.org/10.1029/96jd00932>, 1996.
- Phan, H. M., Ye, Q., Reniers, A. J. H. M., and Stive, M. J. F.: Tidal wave propagation along The Mekong deltaic coast, *Estuar Coast Shelf Sci*, 220, 73–98, <https://doi.org/10.1016/j.ecss.2019.01.026>, 2019.
- Piton, V., Herrmann, M., Lyard, F., Marsaleix, P., Duhaut, T., Allain, D., and Ouillon, S.: Sensitivity study on the main tidal constituents of the Gulf of Tonkin by using the frequency-domain tidal solver in T-UGOm, *Geosci Model Dev*, 13, 1583–1607, <https://doi.org/10.5194/gmd-13-1583-2020>, 2020.
- Qu, T.: Upper-layer circulation in the South China Sea, *J Phys Oceanogr*, 30, 1450–1460, [https://doi.org/10.1175/1520-0485\(2000\)030<1450:ULCITS>2.0.CO;2](https://doi.org/10.1175/1520-0485(2000)030<1450:ULCITS>2.0.CO;2), 2000.
- Qu, T. and Song, Y. T.: Mindoro Strait and Sibutu Passage transports estimated from satellite data, *Geophys Res Lett*, 36, 1–5, <https://doi.org/10.1029/2009GL037314>, 2009.
- Qu, T., Kim, Y. Y., Yaremchuk, M., Tuzuka, T., Ishida, A., and Yamagata, T.: Can Luzon Strait transport play a role in conveying the impact of ENSO to the South China Sea?, *J Clim*, 17, 3644–3657, [https://doi.org/10.1175/1520-0442\(2004\)017<3644:CLSTPA>2.0.CO;2](https://doi.org/10.1175/1520-0442(2004)017<3644:CLSTPA>2.0.CO;2), 2004.
- Qu, T., Du, Y., Meyers, G., Ishida, A., and Wang, D.: Connecting the tropical Pacific with Indian Ocean through South China Sea, *Geophys Res Lett*, 32, 1–4, <https://doi.org/10.1029/2005GL024698>, 2005.
- Qu, T., Du, Y., and Sasaki, H.: South China Sea throughflow: A heat and freshwater conveyor, *Geophys Res Lett*, 33, <https://doi.org/10.1029/2006GL028350>, 2006.
- Ray, R. D. and Zaron, E. D.: M2 internal tides and their observed wavenumber spectra from satellite altimetry, *J Phys Oceanogr*, 46, <https://doi.org/10.1175/JPO-D-15-0065.1>, 2016.
- Rogowski, P., Zavala-Garay, J., Shearman, K., Terrill, E., Wilkin, J., and Lam, T. H.: Air-Sea-Land Forcing in the Gulf of Tonkin: Assessing seasonal variability using modern tools, *Oceanography*, 32, <https://doi.org/10.5670/oceanog.2019.223>, 2019.
- Rojana-anawat, P., Sukramongkol, N., and Pradit, S.: Characteristics of Water in the South China Sea , Area III : Western Philippines, Characteristics of Water in the South China Sea, Area III: Western Philippines, 291–307, 1998.

- 1070 Saadon, M. N., Rojana-Anawat, P., and Snidvongs, A.: Physical Characteristics of Watermass in the South China Sea , Area I : Gulf of Thailand and East Coast of Peninsular Malaysia, Proceedings of the Second Technical Seminar on Marine Fishery Resources Survey in the South China Sea, Area II: Sarawak, Sabah and Brunei Darussalam Waters, 1–5, 1998a.
- Saadon, M. N., Kin, L. P., Snidvongs, A., and Rojana-Anawat, P.: Physical Characteristics of Watermass in the South  
1075 China Sea , Area II : Sarawak, Sabah and Brunei Darussalam Waters, Proceedings of the Second Technical Seminar on Marine Fishery Resources Survey in the South China Sea, Area II: Sarawak, Sabah and Brunei Darussalam Waters, 1–22, 1998b.
- Sannino, G., Herrmann, M., Carillo, A., Rupolo, V., Ruggiero, V., Artale, V., and Heimbach, P.: An eddy-permitting model of the Mediterranean Sea with a two-way grid refinement at the Strait of Gibraltar, *Ocean Model (Oxf)*, 30,  
1080 <https://doi.org/10.1016/j.ocemod.2009.06.002>, 2009.
- Sasaki, H., Kida, S., Furue, R., Aiki, H., Komori, N., Masumoto, Y., Miyama, T., Nonaka, M., Sasai, Y., and Taguchi, B.: A global eddying hindcast ocean simulation with OFES2, *Geosci Model Dev*, 13, <https://doi.org/10.5194/gmd-13-3319-2020>, 2020.
- Shaw, P. T. and Chao, S. Y.: Surface circulation in the South China Sea, *Deep-Sea Research Part I*, 41, 1663–1683,  
1085 [https://doi.org/10.1016/0967-0637\(94\)90067-1](https://doi.org/10.1016/0967-0637(94)90067-1), 1994.
- Shaw, P. T., Chao, S. Y., and Fu, L. L.: Sea surface height variations in the South China Sea from satellite altimetry, *Oceanologica Acta*, 22, 1–17, [https://doi.org/10.1016/S0399-1784\(99\)80028-0](https://doi.org/10.1016/S0399-1784(99)80028-0), 1999.
- Soden, B. J., Lau, N.-C., and Klein, S. A.: Remote Sea Surface Temperature Variations during ENSO: Evidence for a Tropical Atmospheric Bridge, *J Clim*, 12, 917–932, 1999.
- 1090 Sprintall, J., Gordon, A. L., Flament, P., and Villanoy, C. L.: Observations of exchange between the South China Sea and the Sulu Sea, *J Geophys Res Oceans*, 117, 1–18, <https://doi.org/10.1029/2011JC007610>, 2012.
- Susanto, R. D., Wei, Z., Adi, R. T., Fan, B., Li, S., and Fang, G.: Observations of the Karimata Strait throughflow from December 2007 to November 2008, *Acta Oceanologica Sinica*, 32, 1–6, <https://doi.org/10.1007/s13131-013-0307-3>, 2013.
- 1095 Talley, L. D., Pickard, G. L., Emery, W. J., and Swift, J. H.: Descriptive physical oceanography: An introduction: Sixth edition, <https://doi.org/10.1016/C2009-0-24322-4>, 2011.
- Tan, W., Wang, X., Wang, W., Wang, C., and Zuo, J.: Different responses of sea surface temperature in the South China Sea to various El Niño events during boreal autumn, *J Clim*, 29, 1127–1142, <https://doi.org/10.1175/JCLI-D-15-0338.1>, 2016.
- 1100 Tangang, F., Chung, J. X., Juneng, L., Supari, Salimun, E., Ngai, S. T., Jamaluddin, A. F., Mohd, M. S. F., Cruz, F., Narisma, G., Santisirisomboon, J., Ngo-Duc, T., van Tan, P., Singhruck, P., Gunawan, D., Aldrian, E., Sopaheluwakan, A., Grigory, N., Remedio, A. R. C., Sein, D. v., Hein-Griggs, D., McGregor, J. L., Yang, H., Sasaki, H., and Kumar, P.: Projected future changes in rainfall in Southeast Asia based on CORDEX–SEA multi-model simulations, *Clim Dyn*, 55, <https://doi.org/10.1007/s00382-020-05322-2>, 2020.

- 1105 Tian, J., Yang, Q., Liang, X., Xie, L., Hu, D., Wang, F., and Qu, T.: Observation of Luzon Strait transport, *Geophys Res Lett*, 33, 1–6, <https://doi.org/10.1029/2006GL026272>, 2006.
- To Duy, T., Herrmann, M., Estournel, C., Marsaleix, P., Duhaut, T., Bui Hong, L., and Trinh Bich, N.: The role of wind, mesoscale dynamics, and coastal circulation in the interannual variability of the South Vietnam Upwelling, South China Sea - answers from a high-resolution ocean model, *Ocean Science*, 18, [https://doi.org/10.5194/os-18-](https://doi.org/10.5194/os-18-1131-2022)  
1110 1131-2022, 2022.
- Tozuka, T., Qu, T., and Yamagata, T.: Dramatic impact of the South China Sea on the Indonesian throughflow, *Geophys Res Lett*, 34, 3–7, <https://doi.org/10.1029/2007GL030420>, 2007.
- Tozuka, T., Qu, T., Masumoto, Y., and Yamagata, T.: Impacts of the South China Sea Throughflow on seasonal and interannual variations of the Indonesian Throughflow, *Dynamics of Atmospheres and Oceans*, 47, 73–85, <https://doi.org/10.1016/j.dynatmoce.2008.09.001>, 2009.  
1115
- Tozuka, T., Qu, T., and Yamagata, T.: Impacts of South China Sea throughflow on the mean state and El Niño/Southern Oscillation as revealed by a coupled GCM, *J Oceanogr*, 71, 105–114, [https://doi.org/10.1007/s10872-](https://doi.org/10.1007/s10872-014-0265-1)  
014-0265-1, 2015.
- Tranchant, B., Reffray, G., Greiner, E., Nugroho, D., Koch-Larrouy, A., and Gaspar, P.: Evaluation of an operational ocean model configuration at 1/12° spatial resolution for the Indonesian seas (NEMO2.3/INDO12) &ndash; Part 1: Ocean physics, *Geosci Model Dev*, 9, 1037–1064, <https://doi.org/10.5194/gmd-9-1037-2016>, 2016.  
1120
- Trinh, N. B., Marsaleix, P., Estournel, C., Herrmann, M., Ulses, C., Duhaut, T., Shearman, R. K., and To-Duy, T.: High-resolution configuration of the hydrodynamical ocean model SYMPHONIE (version 2.4) over the South China Sea, <https://doi.org/10.5281/ZENODO.7941495>, 2023.
- 1125 Uu, D. v. and Brankart, J. M.: Seasonal variation of temperature and salinity fields and water masses in the Bien Dong (South China) Sea, *Math Comput Model*, 26, 97–113, [https://doi.org/10.1016/S0895-7177\(97\)00243-4](https://doi.org/10.1016/S0895-7177(97)00243-4), 1997.
- Wang, C., Wang, W., Wang, D., and Wang, Q.: Interannual variability of the South China Sea associated with El Niño, *J Geophys Res Oceans*, 111, <https://doi.org/10.1029/2005JC003333>, 2006a.
- Wang, G., Su, J., Ding, Y., and Chen, D.: Tropical cyclone genesis over the south China sea, *Journal of Marine Systems*, 68, 318–326, <https://doi.org/10.1016/j.jmarsys.2006.12.002>, 2007.  
1130
- Wang, Q., Cui, H., Zhang, S., and Hu, D.: Water transports through the four main straits around the South China Sea, *Chinese Journal of Oceanology and Limnology*, 27, 229–236, <https://doi.org/10.1007/s00343-009-9142-y>, 2009.
- Wang, X., Peng, S., Liu, Z., Huang, R. X., Qian, Y. K., and Li, Y.: Tidal mixing in the South China sea: An estimate based on the internal tide energetics, *J Phys Oceanogr*, 46, 107–124, <https://doi.org/10.1175/JPO-D-15-0082.1>, 2016.
- 1135 Wang, Y., Fang, G., Wei, Z., Qiao, F., and Chen, H.: Interannual variation of the South China Sea circulation and its relation to El Niño, as seen from a variable grid global ocean model, *J Geophys Res Oceans*, 111, 1–15, <https://doi.org/10.1029/2005JC003269>, 2006b.
- Wang, Y., Xu, T., Li, S., Susanto, R. D., Agustiadhi, T., Trenggono, M., Tan, W., and Wei, Z.: Seasonal variation of water transport through the Karimata Strait, *Acta Oceanologica Sinica*, 38, 47–57, [https://doi.org/10.1007/s13131-](https://doi.org/10.1007/s13131-018-1224-2)  
1140 018-1224-2, 2019.

- Wang, Y. H., Jan, S., and Wang, D. P.: Transports and tidal current estimates in the Taiwan Strait from shipboard ADCP observations (1999-2001), *Estuar Coast Shelf Sci*, 57, 193–199, [https://doi.org/10.1016/S0272-7714\(02\)00344-X](https://doi.org/10.1016/S0272-7714(02)00344-X), 2003.
- Wei, J., Li, M. T., Malanotte-Rizzoli, P., Gordon, A. L., and Wang, D. X.: Opposite variability of Indonesian throughflow and south China sea throughflow in the Sulawesi Sea, *J Phys Oceanogr*, 46, 3165–3180, <https://doi.org/10.1175/JPO-D-16-0132.1>, 2016.
- 1145
- Wu, C. R. and Hsin, Y. C.: Volume transport through the Taiwan strait: A numerical study, *Terrestrial, Atmospheric and Oceanic Sciences*, 16, 377–391, [https://doi.org/10.3319/TAO.2005.16.2.377\(Oc\)](https://doi.org/10.3319/TAO.2005.16.2.377(Oc)), 2005.
- Wyrтки, K.: Physical Oceanography of the Southeast Asian Waters. Naga Report Volume 2. Scientific Results of Marine Investigation of the South China Sea and the Gulf of Thailand 1959-1961, *Scientific Results of Marine Investigation of the South China Sea and the Gulf of Thailand 1959-1961*, 2, 195, 1961.
- 1150
- Xu, D. and Malanotte-Rizzoli, P.: The seasonal variation of the upper layers of the South China Sea (SCS) circulation and the Indonesian through flow (ITF): An ocean model study, *Dynamics of Atmospheres and Oceans*, 63, 103–130, <https://doi.org/10.1016/j.dynatmoce.2013.05.002>, 2013.
- 1155
- Xu, X., Chassignet, E. P., Wallcraft, A. J., Arbic, B. K., Buijsman, M. C., and Solano, M.: On the Spatial Variability of the Mesoscale Sea Surface Height Wavenumber Spectra in the Atlantic Ocean, *J Geophys Res Oceans*, 127, <https://doi.org/10.1029/2022JC018769>, 2022.
- Xue, H., Chai, F., Pettigrew, N., Xu, D., Shi, M., and Xu, J.: Kuroshio intrusion and the circulation in the South China Sea, *J Geophys Res Oceans*, 109, 1–14, <https://doi.org/10.1029/2002jc001724>, 2004.
- 1160
- Yang, H., Liu, Q., and Jia, X.: On the Upper Oceanic Heat Budget in the South China Sea: Annual Cycle, *Adv Atmos Sci*, 16, 619–629, <https://doi.org/10.1007/s00376-999-0036-x>, 1999.
- Yang, Q., Tian, J., and Zhao, W.: Observation of Luzon Strait transport in summer 2007, *Deep Sea Res 1 Oceanogr Res Pap*, 57, 670–676, <https://doi.org/10.1016/j.dsr.2010.02.004>, 2010.
- Yaremchuk, M., McCreary, J., Yu, Z., and Furue, R.: The South China Sea through flow retrieved from climatological data, *J Phys Oceanogr*, 39, 753–767, <https://doi.org/10.1175/2008JPO3955.1>, 2009.
- 1165
- Yu, K. and Qu, T.: Imprint of the Pacific decadal oscillation on the South China Sea throughflow variability, *J Clim*, 26, <https://doi.org/10.1175/JCLI-D-12-00785.1>, 2013.
- Yu, L. and Weller, R. A.: Objectively analyzed air-sea heat fluxes for the global ice-free oceans (1981-2005), *Bull Am Meteorol Soc*, 88, 527–539, <https://doi.org/10.1175/BAMS-88-4-527>, 2007.
- 1170
- Yu, Y., Zhang, H. R., Jin, J., and Wang, Y.: Trends of sea surface temperature and sea surface temperature fronts in the South China Sea during 2003–2017, *Acta Oceanologica Sinica*, 38, 106–115, <https://doi.org/10.1007/s13131-019-1416-4>, 2019.
- Yu, Z., Shen, S., McCreary, J. P., Yaremchuk, M., and Furue, R.: South China Sea throughflow as evidence by satellite images and numerical experiments, *Geophys Res Lett*, 34, 2–7, <https://doi.org/10.1029/2006GL028103>, 2007.
- 1175
- Yuan, Y., Liao, G., and Yang, C.: The Kuroshio near the Luzon Strait and circulation in the northern South China Sea during August and September 1994, *J Oceanogr*, 64, 777–788, <https://doi.org/10.1007/s10872-008-0065-6>, 2008.

Zeng, L., Timothy Liu, W., Xue, H., Xiu, P., and Wang, D.: Freshening in the South China Sea during 2012 revealed by Aquarius and in situ data, *J Geophys Res Oceans*, 119, <https://doi.org/10.1002/2014JC010108>, 2014.

1180 Zeng, L., Chassignet, E. P., Schmitt, R. W., Xu, X., and Wang, D.: Salinification in the South China Sea Since Late 2012: A Reversal of the Freshening Since the 1990s, *Geophys Res Lett*, 45, <https://doi.org/10.1002/2017GL076574>, 2018.

Zhang, W. Z., Chai, F., Hong, H. S., and Xue, H.: Volume transport through the Taiwan Strait and the effect of synoptic events, *Cont Shelf Res*, 88, 117–125, <https://doi.org/10.1016/j.csr.2014.07.010>, 2014.